Giner-Sanz, JJ.; Ortega Navarro, EM.; Pérez-Herranz, V. (2016). Harmonic analysis based method for linearity assessment and noise quantification in electrochemical impedance spectroscopy measurements: Theoretical formulation and experimental validation for Tafelian systems. Electrochimica Acta. 211:1076-1091. doi:10.1016/j.electacta.2016.06.133.

Harmonic analysis based method for linearity assessment and noise quantification in electrochemical impedance spectroscopy measurements

Theoretical formulation and experimental validation for Tafelian systems

J. J. Giner-Sanz, E. M. Ortega, V. Pérez-Herranz*

IEC group, Depto. Ingeniería Química y Nuclear, Universitat Politècnica de València

Camino de Vera S/N, 46022 Valencia, Spain

*Corresponding author. Tel.: +34-96-3877632; fax: +34-96-3877639;

E-mail address: vperez@iqn.upv.es (V. Pérez-Herranz)

Abstract:

Electrochemical Impedance Spectroscopy (EIS) is an electrochemical measurement technique that has been applied to a broad range of applications. Three conditions must be fulfilled in order to obtain valid EIS measurements: causality, linearity and stationarity. The non fulfilment of any of these conditions may lead to distorted and biased EIS spectra. Consequently, the verification of the four fundamental conditions is mandatory before accepting any results extracted from an EIS spectrum. In this work, a harmonic analysis based method for linearity assessment and noise quantification in EIS measurements is presented, and validated both from an experimental point of view and from a theoretical point of view, for Tafelian systems. It was shown that the presented method was able to quantitatively assess the nonlinearity of the system; and to quantify and characterize the noise. Moreover, the presented method is able to determine the threshold frequency of the system above which the system does not present significant nonlinear effects even for very large perturbation amplitudes.

Keywords: Electrochemical Impedance Spectroscopy (EIS), Harmonic analysis, Tafelian systems, Linearity condition, Noise quantification.

1. Introduction

In recent years, the popularity of the Electrochemical Impedance Spectroscopy (EIS) technique has tremendously increased [1]. This technique, also known as AC impedance method, was initially applied for the determination of double-layer capacitances, and for performing AC polarography [2]. Nowadays it is applied for electrode process characterization and for studying complex interfaces [3]. This electrochemical technique studies the response of a given system to the application of a sinusoidal AC perturbation signal. The measurement is carried out at different perturbation frequencies; hence the name "spectroscopy" [4]. The main strength of this electrochemical technique is that it is able to distinguish the different physic-chemical processes undergoing in the studied system at different timescales [5]. This feature makes the technique suitable for a large range of applications. This explains why it has been widely used in electrochemical related fields as fuel cells [6-12], batteries [13-18], corrosion [19-23], coatings [24-26], electrochemical sensors [27-28] and supercapacitors [29-32]. This electrochemical technique has also been used in fields that are not traditionally related to electrochemistry as biochemical assays [33-36], oncology [37-39] and immunology [40-41], amongst others.

The impedance of a given system is defined by Ohm's generalized law as the ratio between the voltage and the current in the frequency domain [1]:

$$Z(\omega) = \frac{\mathcal{F}[U(t)]}{\mathcal{F}[I(t)]} \qquad (1)$$

where $Z(\omega)$ denotes the complex impedance of the system at angular frequency $\omega = 2\pi f$. $U(t)$ and $I(t)$ respectively stand for the potential and the current signals in the time domain. And finally, $\mathcal{F}$ is the Fourier transform operator. The Fourier transform of an arbitrary function in the time domain, $h(t)$, is defined as [42]:

$$\mathcal{F}[h(t)](\vartheta) = \int_{-\infty}^{+\infty} h(t) \cdot e^{-2\pi j \vartheta t} \cdot dt \qquad (2)$$

Where j denotes the imaginary unit, $\sqrt{-1}$; and ϑ represents the frequency domain independent variable.

The impedance defined in this manner is a complex value. On the one hand, its module gives the ratio between the amplitude of the voltage signal and the amplitude of the current signal: the electric resistance of the system. On the other hand, its argument gives the phase lag of the voltage signal with respect to the current signal. Thus, the

impedance concept is a generalization of the DC electric resistance concept to AC perturbed systems.

The validity of the complex Ohm's law, and thus of the impedance concept, requires the fulfilment of three critical hypotheses: causality, linearity, and stability [43]. If any of these conditions is not met the obtained EIS spectra may be biased, and their analysis may lead to erroneous conclusions on the studied system [44-45]. Therefore, before performing any further analysis on the measured EIS spectra, it is highly advisable to assess if the four critical hypotheses were met during the EIS measurement [46].

A linear system is a system in which the superposition principle holds [47]: the response of a linear system to a linear combination of perturbation signals is a linear combination of the responses of the system to each one of the individual perturbation signals [48]. However, nonlinear effects, such as nonlinear kinetics (Buttler-Volmer's equation) and saturation, often appear in the investigation of electrochemical systems [49]. For this reason, low amplitude perturbations are used in EIS measurements [50], in order to ensure the fulfilment of the linearity condition [51]. Nevertheless, low perturbation amplitudes lead to low signal-to-noise ratios [52]. Consequently, the quality of EIS measurements is given by the trade-off between the linearity condition fulfilment and the maximization of the signal-to-noise ratio [53]: the perturbation amplitude has to be low enough in order to guarantee the fulfilment of the linearity condition [54]; and it has to be high enough in order to achieve an acceptable signal-to-noise ratio [55]. The optimum perturbation amplitude of a given system corresponds with the perturbation amplitude that maximizes the signal-to-noise ratio without violating the linearity condition [56].

A great number of works have studied the effects of the non-fulfilment of the linearity condition: some examples of these works are the works of Darowicki and co-workers [51, 57-59]; the works of Diard and co-workers [60-65]; and the works of Van Gheem's team [66-67]. It has been shown that the main effect of nonlinearity is the generation of non-fundamental harmonics in the output signal [68]. In the case of linear systems, when a mono-frequency sinusoidal perturbation is applied, a mono-frequency sinusoidal output signal of same frequency is obtained [54]. By contrast, when a mono-frequency sinusoidal perturbation is applied to a nonlinear system, the output signal will be composed by a fundamental signal (sinusoidal signal of same frequency than the perturbation signal) with non-fundamental harmonics (sinusoidal signals with frequencies that correspond to integer multiples of the fundamental frequency) superimposed to it [69]. The non-fundamental harmonics generated because of nonlinearity cause a distortion of the measured EIS spectrum that may lead to biased results. Montella and Diard implemented a Wolfram® Demonstration Project [70] that

illustrates very clearly the effects of the nonlinearity of a Tafelian system on the EIS measurements of the system [71].

A great amount of research has been focused in developing techniques to verify the fulfilment of the linearity condition [72]. The linearity assessment methods available in literature can be classified in three main types: the experimental methods; the Kramers-Kronig based methods; and the harmonic analysis based methods [2].

On the one hand, the experimental methods include AC plots, resolution plots and Lissajous figures. These plots allow assessing linearity in real time during the EIS measurement, by directly monitoring the voltage and current raw signals in the time domain [1]. Today, most if not all EIS measurement softwares include this type of tools, which can be displayed during the EIS measurement data acquisition. The main limitation of this type of linearity assessment method is that it is a qualitative method: it is able to detect nonlinearities but it is not able to quantify the nonlinearity level. Moreover, while the distortion of AC plots and Lissajous figures is easily recognizable in the case of severe nonlinearities; the distortion of these plots due to low and moderate nonlinearities may be ambiguous, and its identification can be subjected to the subjectivity of the analyst [1]. Because of this, the use of experimental linearity assessment methods should be reserved for auxiliary experimental validation during the measurement.

On the other hand, Kramers-Kronig relations are integral relations that relate the real part and the imaginary part complex quantities that satisfy the conditions of causality, linearity, stability and finiteness [3]. Numerous works have proven the power of Kramers-Kronig relations as EIS spectra validation tool. An extensive review of the available methods for the application of Kramers-Kronig relations for EIS spectra validation was presented by Agarwal and Orazem [73]. Some examples of Kramers-Kronig based validation methods available in bibliography are the Voight method developed by Boukamp and co-workers [74-75]; and the measurement model method developed by Orazem's group [46, 73, 76-83]. Urquidi-Macdonald and co-workers observed that the Kramers-Kronig relations were highly insensitive to nonlinearity [47]. More recently, it has been shown that Kramers-Kronig relations are only sensitive to nonlinearities if at least part of the spectrum has been measured in a range above a threshold frequency of the system; and even then, the sensitivity is not very high [84]. Consequently, the main limitation of the Kramers-Kronig based linearity assessment methods is their low sensibility [85-86].

Finally, the harmonic analysis based methods assess linearity through the quantification of the non-fundamental harmonic content in the response signal. These methods are based in the analysis of the system's response in the frequency domain.

Several examples of this type of linearity assessment method are available in literature, such as the method developed by Popkirov and Schindler [44-69], and the Pintelon's team method [87-88]. This type of linearity assessment methods has a double advantage over the other two types: they are quantitative methods, and therefore they are able to quantify the level of nonlinearity in an objective manner; and they have a great sensibility to nonlinearities [89].

The aim of this work is to develop a quantitative linearity assessment method for EIS measurements, based on the analysis of the system's response in the frequency domain. The presented method is able to quantify both, the nonlinearity of the system and the noise in the measurement: therefore, one of its immediate applications can be the optimization of the perturbation amplitude for EIS measurements. Thought the developed method can be applied to any electrochemical system, this work will focus on Tafelian systems. In this paper, both the theoretical foundation and the experimental validation of the method are presented. The experimental validation of the method was performed using a known Tafelian system: an alkaline hydrogen evolution electrochemical cell.

2. Linearity assessment method

The linearity assessment method implemented in this work consists in three main steps. First, the EIS spectrum is recorded in the traditional way. However, instead of saving only the impedance value for each excited frequency, as it is usually done; the raw current and voltage signals in the time domain, $I(t)$ and $U(t)$, are also stored for each frequency. In the second step of the method, the current and voltage signals in the frequency domain, $\hat{I}(\vartheta)$ and $\hat{U}(\vartheta)$, are obtained for each excited frequency. This step is accomplished by using a Fast Fourier Transform (FFT) algorithm that transforms the signals in the time domain into the frequency domain. This algorithm is an efficient algorithm to compute the discrete Fourier transform of a discretized signal in the time domain [90]:

$$\widehat{\mathrm{X}}_{\mathrm{i}} = \sum_{\mathrm{k}=0}^{\mathrm{N}-1} \mathrm{x}_{\mathrm{k}} \cdot \mathrm{e}^{-\frac{2\pi \mathrm{j}}{\mathrm{N}} \mathrm{k} \cdot \mathrm{i}} \qquad (3)$$

where N stands for the number of samples acquired during the discretization of the signal in the time domain; $\{\mathrm{x}\}$ denotes the series of the discretized signal in the time domain; and $\{\widehat{\mathrm{X}}\}$ is the series of the Fourier transform in the frequency domain. In this case, a discrete Fourier transform is used since the signals in the time domain are discrete (digital measurement).

Once the signals have been transformed to the frequency domain, the level of non-fundamental harmonics in each one of the signals must be quantified. In this work, the following parameter was used in order to quantify the level of non-fundamental harmonics in signal X (current or voltage):

$$\wp X = \max_{\mathrm{k}\neq 1} \; 20 \cdot \log_{10}\left(\frac{\left|\hat{X}\right|_k}{\left|\hat{X}\right|_1}\right) \qquad (4)$$

where $\left|\hat{X}\right|$ denotes the amplitude of the Fourier transform of signal X. Subscript 1 refers to the fundamental component of the signal, whereas subscripts greater or equal to 2 refer to non-fundamental harmonics of the signal. This parameter quantifies in decibels (dB) the ratio between the most important non-fundamental harmonic of the signal, and its fundamental component.

The third step of the linearity assessment method consists in quantifying the level of non-fundamental harmonics in each signal: parameters $\wp I$ and $\wp U$ are calculated for each excited frequency, using the following expressions:

$$\wp I = \max_{k\neq 1} \; 20 \cdot \log_{10}\left(\frac{\left|\hat{I}\right|_k}{\left|\hat{I}\right|_1}\right) \tag{5}$$

$$\wp U = \max_{k\neq 1} \; 20 \cdot \log_{10}\left(\frac{\left|\hat{U}\right|_k}{\left|\hat{U}\right|_1}\right) \tag{6}$$

Therefore, after applying the proposed method, the values of parameters $\wp I$ and $\wp U$ are obtained for each one of the frequencies at which the impedance was measured in the first step. These results can be analyzed using two tools: the $\wp X$ curves and the critical parameters. On the one hand, the $\wp X$ curves correspond with the representation of parameters $\wp I$ and $\wp U$ versus the excited frequency. These curves allow to evaluate linearity for each frequency individually. Therefore, these curves are very useful for distinguishing for which frequencies the studied system is more susceptible to present nonlinearities. On the other hand, the critical parameters correspond with the parameters $\wp I$ and $\wp U$ at the critical frequency. The critical frequency being defined as the excitation frequency with the highest harmonic content. Consequently, the critical parameters, $\wp I_{\mathrm{c}}$ and $\wp U_{\mathrm{c}}$, are given by the following expressions:

$$\wp I_{\mathrm{c}} = \max_{i\epsilon\{1;2;\cdots;N_f\}} \wp I_{\mathrm{i}} \tag{7}$$

$$\wp U_{\mathrm{c}} = \max_{i\epsilon\{1;2;\cdots;N_f\}} \wp U_{\mathrm{i}} \tag{8}$$

where N_f denotes the number of frequencies at which the impedance was measured. These critical parameters provide an overall assessment of linearity by considering the most unfavorable frequency: the frequency of the EIS spectrum with the highest harmonic content.

Figure 1 gives the outline of the proposed linearity assessment method. As it can be seen in the mentioned figure, for a given EIS spectrum two $\wp X$ curves and two critical parameters are obtained (one for the current signal and one for the voltage signal). This linearity assessment method can be easily automated in any programming language. In this work it was fully implemented in Labview®. The developed Labview® program directly takes as input the output of the software used for controlling the impedance measurement system, Nova®. Nova®'s output consists in the digitalized raw signals (current and voltage) in the time domain; and the transformed signals in the frequency domain (Nova® applies internally an FFT algorithm). The implemented Labview® program reads the transformed signals in the frequency domain; and then, it calculates parameters $\wp I$ and $\wp U$. This process is repeated for each one of the frequencies at which the impedance is measured.

3. Experimental

As it was stated in the introduction section, one of the aims of this work is to experimentally validate the implemented linearity assessment method, presented in section 2. Therefore, the goal is to determine whether the method is able to detect and quantify nonlinearities, or not. The experimental validation should be performed over a large range of nonlinearities. Thus, a highly nonlinear electrochemical system should be used for performing the experimental validation; since for this kind of electrochemical system, a slight increase in the perturbation amplitude causes a large increase in the nonlinearity of the system. Consequently, this type of electrochemical system allows to obtain a wide range of nonlinearities just by increasing the applied perturbation amplitude. In addition, as it was mentioned in the introduction section, this work focuses on Tafelian systems. Therefore, the selected experimental system should be a highly nonlinear Tafelian system. Using these selection criteria, the experimental system selected for this work was the cathodic electrode of an alkaline water electrolyser. According to the works of Herraiz-Cardona and co-workers [91-93], this electrochemical system corresponds to a highly nonlinear Tafelian system. A detailed description of the system is presented by Herraiz-Cardona [91].

Figure 2 illustrates the experimental setup used to perform the experimental validation of the implemented linearity assessment method. The main element of this setup is an electrochemical cell patented by the Dpto. Ingenieria Quimica y Nuclear of Universitat Politècnica de València (Spain) [95]. It consists in a three-electrode electrochemical cell coupled to a heating water circuit that allows controlling the temperature of the cell.

On the one hand, one of the electrodes developed by Herraiz-Cardona and co-workers was used as the working electrode. The working electrode was placed in one of the two horizontal positions available in the electrochemical cell. It consists in a nickel electrode produced at very high current densities using the procedure described in [92]. The geometric area of the electrode used in this work was of 0.5 cm^2. On the other hand, the counter-electrode was placed in one of the three vertical openings available in the electrochemical cell. In this work, a nickel foam with very high surface area (Incofoam® 0.17 cm thick and 50 pores per linear inch) was used as counter-electrode. Finally, a commercial Ag/AgCl (3M KCl) electrode was used as the reference electrode, which was placed in another of the three vertical openings of the electrochemical cell. The third vertical opening was left open to the atmosphere, in order to act as a gas vent; and thus, to prevent overpressures inside the electrochemical cell due to the gases produced during the water electrolysis. An oxygen free 30 wt.% KOH solution was used as electrolyte. Before each experimental session, fresh electrolyte was prepared using 85 wt.% KOH Panreac® lentils. To avoid

the carbonation of the electrolytic solution, which would cause an increase of the electrolyte resistance over time, the electrolyte was deaerated by bubbling nitrogen for 15 minutes just before starting the experiments.

In order to perform the experimental validation of the linearity assessment method, the EIS spectrum of the system has to be obtained for different degrees of nonlinearity. As introduced above, different degrees of nonlinearity may be obtained by using different perturbation amplitudes. Therefore, in this work, the EIS spectrum of the system was measured using 12 different perturbation amplitudes (peak to peak): 0.1 mA; 0.5 mA; 1 mA; 2 mA; …; 10 mA. All the experiments were carried out at 30°C, in galvanostatic mode. In preliminary works, it was observed that the most nonlinear operation point of the system is obtained for an operation DC current of -10 mA, which corresponds to an overvoltage of around -200 mV. The minus sign indicates that the working electrode acts as the cathode of the system. As it was stated previously, a high nonlinear behaviour is desired for the experimental validation of the linearity assessment method, since it maximizes the change in nonlinearity for a given change in the perturbation amplitude. For this reason, all the experiments were performed at a DC current of -10 mA. The maximum perturbation amplitude of 10 mA was selected in order to guarantee that the working electrode acts as the cathode of the cell during the whole EIS measurement, even for the maximum perturbation amplitude.

The EIS measurements were performed using an Autolab® 302N potentiostat/galvanostat with FRA module, controlled using NOVA® software. The measurement frequency range was 10 kHz – 5 mHz, with 10 frequencies per decade. Table 1 lists the measurement parameters used for all the measurements. The meaning of each one of these measurement parameters was widely explained in a previous work [96].

Before each experiment, a pre-treatment was applied to the working electrode in order to ensure similar surface conditions in all experiments. The applied pre-treatment consisted in applying a -1.6V vs. Ag/AgCl potential (this corresponds to an overvoltage of around -350 mV) during 30 minutes. This treatment was done to reduce any oxide film that could exist on the surface of the porous electrode [93], in order to guarantee that the surface of the electrode was in similar conditions in all the experiments. This pre-treatment is critical in order to ensure the reproducibility of the results from one experiment to another.

4. Results

The methodology outlined in section 2 was applied to each one of the experimental spectra obtained using different perturbation amplitudes, as described in the experimental methodology section. In this section, the obtained experimental results are presented. Since this work focuses on a linearity assessment method and not on the effect of nonlinearity on the impedance measurement, the impedance results were omitted. If needed, the impedance results of this work were presented and thoroughly discussed in a previous paper [89].

4.1. $\wp X$ curves

Figures 3 and 4 show the obtained $\wp X$ curves for the perturbation signal and for the output signal respectively. These curves consist in the representation of the $\wp X$ value obtained using equations (5) and (6) ($\wp I$ for the perturbation signal; and $\wp U$ for the output signal) versus the perturbation signal frequency. Each figure is divided in two parts: subfigure (a) shows the $\wp X$ curves obtained for low perturbation amplitudes; whereas, subfigure (b) shows the $\wp X$ curves obtained for high perturbation amplitudes.

On the one hand, in figure 3 it can be observed that the $\wp I$ curves present the same pattern for all the perturbation amplitudes. For a given perturbation amplitude, the $\wp I$ parameter is approximately constant for high perturbation amplitudes. A little $\wp I$ peak is observed in the intermediate frequency range, ranging from $10\ Hz - 0.1\ Hz$. And finally, the $\wp I$ parameter stabilizes for low perturbation frequencies, around a slightly higher value than the high frequency value. In figure 3.a it can be observed that for low perturbation amplitudes, an increase in the perturbation amplitude shifts the $\wp I$ curve to lower values. In contrast, as it can be observed in figure 3.b, for perturbation amplitudes larger than 2 mA, an increase in the perturbation amplitude has no significant effect on the $\wp I$ curve. When the potentiostat was used to perform measurements in a different system (i.e. PEM fuel cell) exactly the same $\wp I$ curves were obtained [56]: this indicates that these $\wp I$ curves are characteristic of the measurement equipment, which is responsible for generating the perturbation, and applying it to the system. These curves may be affected by distortions in the grid signal that powers the measurement equipment, and by electric couplings between the measurement equipment and other devices connected to the same electrical grid. For low perturbation amplitudes, an increase in the perturbation amplitude leads to an improvement of the signal-to-noise ratio, which causes a drop in the $\wp I$ parameter according to equation (5): this effect explains the trend observed in figure 3.a. However, there is a threshold amplitude (around 2 mA, in this case) above which further increases in the perturbation amplitude do not improve the signal-to-noise

ratio anymore, since the limit of the measurement system has been reached. Beyond this perturbation amplitude, the $\wp I$ parameter does not decrease further with the perturbation amplitude, resulting in the nearly superimposed $\wp I$ curves with no clear trend with the perturbation amplitude, as seen in figure 3.b.

On the other hand, in figure 4 it can be observed that the overall shape of the $\wp U$ curves changes from low perturbation amplitudes (figure 4.a) to high perturbation amplitudes (figure 4.b). For low perturbation amplitudes (up to 2 mA, in this case), the $\wp U$ curve for a given perturbation amplitude is a point cloud with no clear trend or shape, that presents peaks at given perturbation frequencies. The $\wp U$ values are significantly higher in the intermediate frequency range from 100 Hz to 1 Hz. It can also be observed, that an increase in the perturbation amplitude for amplitudes below 2 mA causes a shift of the $\wp U$ curve towards lower values of $\wp U$. This is due to the improvement of the signal-to-noise ratio.

As it can be observed in figure 4.b, for high perturbation amplitudes (above 2 mA) a clear shape appears in the $\wp U$ curves. For a given perturbation amplitude, three distinct zones can be identified in the $\wp U$ curve:

- For high perturbation frequencies, the $\wp U$ curve is nearly horizontal, except for peaks that appear at defined perturbation frequencies. Probably, these peaks are due to the coupling of the system with the electric grid;
- For intermediate perturbation frequencies, the $\wp U$ curve is monotonically increasing and presents an inflexion point. Moreover, some peaks at defined frequencies appear also in this frequency range. As in the previous case, it is probable that these peaks are due to the coupling of the system with the electric grid;
- Finally, the $\wp U$ curve shows an asymptotic behavior for low perturbation frequencies. In this frequency range, no peaks are observed.

Comparing the $\wp U$ curves for different perturbation amplitudes, at high perturbation amplitude, it can be observed that the $\wp U$ curves shift to higher $\wp U$ values with an increase in the perturbation amplitude. This trend is due to the nonlinear effects of the system. For high perturbation amplitudes (higher than a threshold amplitude), the nonlinear effects of the system are no longer negligible: an increase in the perturbation amplitude causes greater nonlinear effects, that cause an increase of the amplitude of the non fundamental harmonics in the output signal, and this results in a higher $\wp U$ value according to equation (6). From figure 4.b it can be deduced that the nonlinear effects appear mainly for low perturbation frequencies (lower than a threshold frequency). The existence of a frequency threshold above which nonlinearities are negligible even for high perturbation amplitudes was already

observed by Hirschorn and co-workers [53, 84]. The overall shape of the $\wp U$ curves, in the nonlinear zone (high perturbation amplitudes), experimentally obtained in this work are consistent with the theoretical curves obtained by Lai [68].

In short: for amplitudes lower than the amplitude threshold of the system, an increase in the perturbation amplitude causes a shift of the $\wp U$ curve towards lower $\wp U$ values; while for amplitudes higher than the amplitude threshold of the system, an increase in the perturbation amplitude causes a shift of the $\wp U$ curve towards higher $\wp U$ values, for frequencies lower than a frequency threshold. Moreover, for perturbation amplitudes higher than the threshold amplitude, a defined shape appears in the $\wp U$ curves. The effect of the perturbation amplitude on the $\wp U$ curves is given by the balance of two antagonist effects: on the one hand, an increase in the perturbation amplitude improves the signal-to-noise ratio; on the other hand, an increase in the perturbation amplitude leads to higher nonlinear effects that cause the generation of higher non fundamental harmonics in the output signal. For low amplitudes (lower than the threshold amplitude), the non fundamental harmonics generated on account of the nonlinear effects of the system are negligible. Thus, in this amplitude range, the noise dominates over the nonlinear effects. On the contrary, for high amplitudes (higher than the threshold amplitude), nonlinear effects dominate over the noise. Therefore, the net effect of an increase in the perturbation amplitude at high amplitudes is an increase of the $\wp U$ value, for frequencies lower than a frequency threshold. For frequencies above this frequency threshold, the system does not present nonlinear effects even for high perturbation amplitudes. Thus, for high frequencies, an increase in the perturbation amplitude always causes a decrease in the $\wp U$ value. This can be observed in the peaks at high and intermediate frequencies that appear in figure 4.b: even for high perturbation amplitudes, an increase in the perturbation amplitude causes a drop in the peak height.

Comparing figures 3 and 4, it can be observed that the $\wp X$ values associated to the output signal are significantly larger than the values associated to the input signal. It can be deduced that the major part of the harmonics present in the output signal (due to both, noise and nonlinear effects) are generated by the system itself, since they are only present in the output signal. In addition, it can be also deduced that the harmonic generation due to nonlinear effects only occurs in the output signal; there is no back resonance that would introduce harmonics in the perturbation signal due to the electrical coupling between the measurement system and the measured system. Therefore, only the output signal is relevant for linearity assessment. However, it is advisable to monitor also the perturbation signal, in order to control the quality of the perturbation signal and to detect possible distortions in the grid that could introduce noise in the measurements.

It should be noted that if the EIS measurements were performed in potentiostatic mode, rather than in galvanostatic mode as they were done in this work, the results would be reversed: the $\wp X$ values of the current signal would be significantly higher than the $\wp X$ values of the voltage signal. Thus, in potentiostatic mode, $\wp I$ contains the information of the noise and the nonlinear effects; whereas, in galvanostatic mode, it is $\wp U$ which contains this information.

4.2. Critical parameters

Figures 5 and 6 present the critical parameter curves for the perturbation signal and the response signal respectively. These curves correspond with the representation of the critical parameter ($\wp I_{\mathrm{c}}$ and $\wp U_{\mathrm{c}}$) versus the amplitude of the applied perturbation. Next to each point, the critical frequency for that perturbation amplitude is displayed.

Comparing the scales of figures 5 and 6, it can be observed that the $\wp U_{\mathrm{c}}$ are significantly higher than the $\wp I_{\mathrm{c}}$ values for all perturbation amplitudes. This is due to the fact that the system introduces additional noise; and for high perturbation amplitudes it also introduces non fundamental harmonics due to nonlinear effects. The result is that the critical parameter associated with the perturbation signal is significantly lower than the critical parameter associated to the output signal, for a given perturbation amplitude.

On the one hand, in figure 5 it can be observed that for very low perturbation amplitudes an increase in the perturbation amplitude causes a drop of the $\wp I_{\mathrm{c}}$ value. On the contrary, for perturbation amplitudes higher than 0.5 mA, $\wp I_{\mathrm{c}}$ remains approximately constant around -60. When the perturbation amplitude is increased the signal-to-noise ratio of the perturbation signal improves, resulting in a drop of the critical parameter $\wp I_{\mathrm{c}}$. Once the limit of the measurement equipment that generates the perturbation signal is reached, further increases of the perturbation amplitude do not improve further the signal-to-noise ratio.

On the other hand, two different trends can be observed in figure 6. For low perturbation amplitudes, an increase in the amplitude causes a drop of the critical parameter of the output signal, $\wp U_{\mathrm{c}}$; whereas, at high amplitudes, an increase in the perturbation amplitude causes an increase in $\wp U_{\mathrm{c}}$. The perturbation amplitude at which the trend of parameter $\wp U_{\mathrm{c}}$ inverts is defined as the critical amplitude of the system, ΔI_c. The critical amplitude concept is consistent with the threshold amplitude concept identified in section 4.1. An increase in the perturbation amplitude causes two antagonist effects. On the one side, an increase in the amplitude improves the signal-to-noise ratio. On the other side, an increase in the perturbation amplitude generates higher levels of non fundamental harmonics due to nonlinear effects of the system. For

amplitudes below the critical amplitude, the first effect dominates over the second one: the net effect of an increase of the perturbation amplitude for low amplitudes is a drop in $\wp U_c$; and therefore, the system can be considered to behave linearly-like in this perturbation amplitude range. The amplitude range below the critical amplitude corresponds with the linear behaviour zone, identified in figure 6. In contrast, for amplitudes above the critical perturbation amplitude, the second effect dominates over the first one: the net effect of an increase of the perturbation amplitude in this amplitude range is an increase in $\wp U_c$; and thus, the nonlinear behaviour of the system is significant for perturbation amplitudes above the critical amplitude. The amplitude range above the critical amplitude corresponds with the nonlinear behaviour zone, identified in figure 6.

The critical perturbation amplitude delimits the linear behaviour zone of the system, and its nonlinear behaviour zone. The critical perturbation amplitude can be experimentally determined from the critical parameter curve. In this case, it can be deduced from figure 6: the critical perturbation amplitude of the studied system (in the operation conditions at which it was operated in this work) is around 2 mA.

Finally, in figure 6 it can be observed that the critical frequency changes from one zone to the other. On the one side, for all the perturbation amplitudes in the linear behaviour zone, the critical frequency is 25 Hz. This frequency is the perturbation frequency that presents a higher noise level in the system: therefore, in the linear behaviour zone (where noise is dominant over nonlinear effects) the critical frequency corresponds with the frequency with a higher noise level. On the other side, the critical frequency is of 5 mHz (the lowest frequency in the measured frequency range) for every perturbation amplitude in the nonlinear behaviour zone. This is consistent with the fact that nonlinear effects only appear for low frequencies (below a frequency threshold): therefore, in the nonlinear zone (where nonlinear effects are dominant over noise) the critical frequency is the minimum measured frequency, which is the frequency that exhibits higher nonlinear effects. Consequently, the change in the critical frequency is an indicator of the domination switch from noise to nonlinear effects.

5. Theoretical modelling

5.1. Model definition

In general, the input signal for EIS measurements is considered as a mono-frequency sinusoidal signal with negligible levels of noise. This assumption is consistent with the experimental observations presented in section 4.1; and consequently it was considered in this work. According to this assumption, the perturbation signal can be written as:

$$\mathrm{I(t)} = \mathrm{I_{DC}} + \Delta\mathrm{I} \cdot \sin(\omega \mathrm{t}) \qquad (9)$$

where $\mathrm{I_{DC}}$ denotes the polarization current. By convention, the perturbation amplitude, $\Delta\mathrm{I}$, is a nonzero positive number. When this perturbation signal is applied to the electrochemical system an output signal is obtained. The output signal consists in a superposition of sinusoidal signals: a fundamental signal and its harmonics. Each one of these signals is composed of two contributions. One contribution is due to the response of the system: the response of the system in the fundamental frequency is associated to its linear response; whereas, the response of the system in the non fundamental frequencies is associated to its nonlinear response. And the other contribution is associated to the noise. Consequently, the output signal can be expressed as:

$$U(t) = U_{DC} + (\Delta U_1 + \Delta U_{n1}) \cdot \sin(\omega t + \varphi_1) + \sum_{k=2}^{+\infty} (\Delta U_k + \Delta U_{nk}) \cdot \sin(k\omega t + \varphi_k) \qquad (10)$$

where U_{DC} denotes the DC component of the output signal. On the one hand, ΔU_1 denotes the contribution of the linear response of the system to the fundamental component of the output signal; and ΔU_{n1} stands for the noise in the fundamental component of the output signal. On the other hand, ΔU_k and ΔU_{nk} (for $k \geq 2$) denote respectively the system's response and the noise in the k-th harmonic. Finally, φ_k (for $k \geq 1$) denotes the phase-lag of the k-th component of the output signal with respect to the perturbation signal. Figure 7 summarizes the assumed situation.

Two different cases are considered:

- Case 1: $\Delta\mathrm{I} \leq \Delta\mathrm{I_c}$. The perturbation amplitude is below the critical perturbation amplitude, and therefore, the system is in the linear behaviour zone. The critical frequency of the system in this case is referred to as the critical frequency of the linear behaviour zone, f_{c_linear};

- Case 2: $\Delta \mathrm{I} > \Delta \mathrm{I_c}$. The perturbation amplitude is above the critical perturbation amplitude, and therefore, the system is in the nonlinear behaviour zone. The critical frequency of the system in this case is referred to as the critical frequency of the nonlinear behaviour zone, $f_{c\_nonlinear}$.

5.2. Case 1: Linear behaviour zone

As described in detail in the previous section, in the linear behaviour zone, the nonlinear effects of the system are negligible in comparison to the noise. Therefore, in this region:

$$\Delta U_k \ll \Delta U_{nk} \ \ \forall k \in \mathbb{N} | k \neq 1 \tag{11}$$

Moreover, it can be assumed with no loss of generality that the fundamental component of the output signal is high enough in order to overcome the noise associated to it; otherwise, the measurement would be only noise. Thus, it can be considered that:

$$\Delta U_1 \gg \Delta U_{n1} \tag{12}$$

Introducing assumptions (11) and (12) in equation (10), and particularizing the obtained expression for a perturbation frequency of f, the following expression is obtained:

$$\begin{aligned} U(t) = U_{DC} &+ \Delta U_1(f) \cdot \sin\big(2\pi f t + \varphi_1(f)\big) \\ &+ \sum_{k=2}^{+\infty} \Delta U_{nk}(f) \cdot \sin\big(2k\pi f t + \varphi_k(f)\big) \end{aligned} \tag{13}$$

Applying the definition of Fourier's transform to equation (13), the following expressions are obtained:

$$\left|\widehat{U}\right|_1 = \Delta U_1 \tag{14}$$

$$\left|\widehat{U}\right|_k = \Delta U_{nk} \ \ \forall k \in \mathbb{N} | k \neq 1 \tag{15}$$

Introducing these expressions in the definition of $\wp U$ presented in section 2, the following expression is obtained for the parameter $\wp U$ for a perturbation frequency f:

$$\wp U(f) = \max_{k\neq 1} \; 20 \cdot \log_{10}\left(\frac{\Delta U_{nk}(f)}{\Delta U_1(f)}\right) \qquad (16)$$

Applying the properties of the maximum operator:

$$\wp U(f) = 20 \cdot \log_{10}\left(\frac{\max\limits_{k\neq 1} \; \Delta \mathrm{U_{nk}}(f)}{\Delta \mathrm{U}_1(f)}\right) \qquad (17)$$

The following parameter is defined:

$$\Delta \mathrm{U_{noise}}(f) = \max_{h\neq 1} \; \Delta \mathrm{U_{nh}}(f) \qquad (18)$$

This parameter, with dimensions of voltage, corresponds with the amplitude of the non fundamental harmonic associated to noise with the highest amplitude. This parameter is a measure of the noise level at frequency f. It is assumed that the noise level at frequency f is independent of the perturbation amplitude: according to this assumption, parameter $\Delta \mathrm{U_{noise}}$ does not depend on $\Delta \mathrm{I}$.
In addition, according to Ohm's generalized law, the linear component of the system's response is given by:

$$\Delta \mathrm{U}_1(f) = |\mathrm{Z(f)}| \cdot \Delta \mathrm{I} \qquad (19)$$

where $|\mathrm{Z(f)}|$ denotes the modulus of the impedance of the system at frequency f. Introducing equations (18) and (19) in (17):

$$\wp U(f) = 20 \cdot \log_{10}\left(\frac{\Delta \mathrm{U_{noise}}(f)}{|\mathrm{Z(f)}| \cdot \Delta \mathrm{I}}\right) \qquad (20)$$

Applying the properties of logarithms, the following expression is obtained for the parameter $\wp U$ for a perturbation frequency f:

$$\wp U(f) = c_1 \cdot ln\left(\frac{1}{\Delta I}\right) + c_2(f) \qquad (21)$$

where:

$$c_1 = \frac{20}{\ln(10)} \qquad (22)$$

$$c_2(f) = \frac{20}{\ln(10)} \cdot ln\left(\frac{\Delta U_{noise}(f)}{|Z(f)|}\right) \quad (23)$$

It can be concluded that parameter $\wp U(f)$ follows a logarithmic relation with the inverse of the perturbation amplitude. The constant term of the relation being related to the noise-level-related parameter $\Delta U_{noise}(f)$, at the corresponding frequency. The constant term, $c_2(f)$, incorporates the noise level at frequency f; and the impedance modulus of the system at that frequency. Therefore, this parameter quantifies the effective level of noise at frequency f. Consequently, $c_2(f)$ is the effective noise parameter at frequency f. Expression (23) encapsulates the improvement of the signal-to-noise ratio obtained by increasing the perturbation amplitude when the noise level is constant with the perturbation amplitude.

By the definition of the critical parameter introduced in section 2, $\wp U_c$ corresponds with the parameter $\wp U(f)$ at the critical frequency. Expression (21) is applicable to any perturbation frequency f; thus, it can be applied to the critical frequency of the linear behaviour zone (f_{c_linear}) in order to obtain an expression for the critical parameter $\wp U_c$:

$$\wp U_c = \wp U(f_{c\_linear}) = \frac{20}{\ln(10)} \cdot ln\left(\frac{1}{\Delta I}\right) + c_2(f_{c\_linear}) \quad (24)$$

This model, which only has one fitting parameter (c_2), was fitted to the linear behaviour zone of the experimental $\wp U_c$ curve, presented in section 4.2. The fitting process was performed using a Levenberg-Marquardt algorithm implemented in Labview®. The obtained fitting is shown in figure 8. It can be observed that the model given by equation (24) fits perfectly the experimental $\wp U_c$ curve in the linear behaviour zone: the associated determination coefficient being of 99.93%. It can be deduced that the proposed model actually explains the experimental shape of the $\wp U_c$ curve in the linear behaviour zone. This confirms the assumption that the noise level at frequency f is independent of the perturbation amplitude, at least for the critical frequency of the linear behaviour zone. From the experimental fit, the value of $c_2\left(f_{c\_linear}\right)$ can be obtained:

$$c_2\left(f_{c\_linear}\right) = \frac{20}{\ln(10)} \cdot ln\left(\frac{\Delta U_{noise}\left(f_{c\_linear}\right)}{\left|Z\left(f_{c\_linear}\right)\right|}\right) = -19.8\ dB \quad (25)$$

In this case, the modulus of the impedance of the system at frequency f_{c_linear} is 1.86Ω. Using this value in expression (25), the value of $\Delta U_{noise}(f_{c\_linear})$ can be estimated:

$$\Delta \mathrm{U}_{\mathrm{noise}}\left(f_{c\_linear}\right) = \left|\mathrm{Z}\left(f_{c\_linear}\right)\right| \cdot 10^{\frac{c_2\left(f_{c\_linear}\right)}{20}} \approx 0.191\mathrm{V} \qquad (26)$$

This value quantifies the noise level in the critical frequency of the linear behaviour zone. Therefore, the noise level can be quantified from the linear behaviour zone of the $\wp U_{\mathrm{c}}$ curve.

5.3. Case 2: Nonlinear behaviour zone

In contrast with the linear behaviour zone described in the previous subsection, in the nonlinear behaviour zone the nonlinear effects of the system are not negligible in comparison to the noise. Since the amplitude of the non fundamental harmonics decreases with the harmonic order [71], it can be assumed without loss of generality that only the first $\mathrm{k}_{\mathrm{lim}} \geq 2$ harmonics overcome the noise in the corresponding frequency. Therefore, in the nonlinear behaviour region:

$$\Delta \mathrm{U}_{\mathrm{k}} \gg \Delta \mathrm{U}_{\mathrm{nk}} \qquad \forall \mathrm{k} \in \mathbb{N} | \mathrm{k} \leq \mathrm{k}_{\mathrm{lim}} \ \text{ with } \mathrm{k}_{\mathrm{lim}} \in \mathbb{N} | \mathrm{k}_{\mathrm{lim}} \geq 2 \qquad (27)$$

$$\Delta \mathrm{U}_{\mathrm{k}} \ll \Delta \mathrm{U}_{\mathrm{nk}} \qquad \forall \mathrm{k} \in \mathbb{N} | \mathrm{k} > \mathrm{k}_{\mathrm{lim}} \ \text{ with } \mathrm{k}_{\mathrm{lim}} \in \mathbb{N} | \mathrm{k}_{\mathrm{lim}} \geq 2 \qquad (28)$$

Note that this set of conditions already incorporates the assumption that the fundamental component ($\mathrm{k} = 1$) overcomes the noise associated to it.

Introducing assumptions (27) and (28) in equation (10), and particularizing the obtained expression for the critical frequency of the nonlinear behaviour zone $\left(f_{c\_nonlinear}\right)$, the following expression is obtained:

$$\begin{aligned} U(t) = U_{DC} &+ \Delta U_1 \cdot \sin\left(2\pi f_{c\_nonlinear} t + \varphi_1\right) \\ &+ \sum_{k=2}^{k_{lim}} \Delta U_k \cdot \sin\left(2k\pi f_{c\_nonlinear} t + \varphi_k\right) \\ &+ \sum_{k=k_{lim}+1}^{+\infty} \Delta U_{nk} \cdot \sin\left(2k\pi f_{c\_nonlinear} t + \varphi_k\right) \end{aligned} \qquad (29)$$

Applying the definition of Fourier's transform to equation (29), the following expressions are obtained:

$$\left|\widehat{U}\right|_1 = \Delta U_1 \qquad (30)$$

$$\left|\widehat{U}\right|_k = \Delta U_k \ \ \forall k \in \mathbb{N} | k \in [2; \mathrm{k}_{\mathrm{lim}}] \qquad (31)$$

$$\left|\widehat{U}\right|_k = \Delta U_{nk} \;\; \forall k \in \mathbb{N} | k > \mathrm{k_{lim}} \qquad (32)$$

Introducing these expressions in the definition of $\wp U$ presented in section 2, the following expression is obtained for the critical parameter $\wp U_\mathrm{c}$ (since equation (29) was particularized for the critical frequency of the nonlinear behaviour zone, the corresponding $\wp U$ parameter defines the critical parameter $\wp U_\mathrm{c}$):

$$\wp U_\mathrm{c} = 20 \cdot \log_{10}\left(\frac{max\{\Delta U_k \; with \; k \in [2; \mathrm{k_{lim}}]; \Delta U_{nk} \; with \; k > \mathrm{k_{lim}}\}}{\Delta U_1}\right) \qquad (33)$$

On the one hand, according to the fact that the amplitude of the non fundamental harmonics decreases with the harmonic order: $\Delta U_2 \geq \Delta U_k \; \forall k \in \mathbb{N} | k \in [2; \mathrm{k_{lim}}]$. On the other hand, according to the definition of the nonlinear behaviour zone introduced in section 5.1, in this region the nonlinear effects are not negligible with respect to noise. Therefore it can be assumed that in this case: $\Delta U_2 \geq \Delta U_{nk} \; \forall k \in \mathbb{N} | k > \mathrm{k_{lim}}$. Introducing these assumptions in equation (33), the following relation is obtained:

$$\wp U_\mathrm{c} = 20 \cdot \log_{10}\left(\frac{\Delta \mathrm{U_2}}{\Delta \mathrm{U_1}}\right) \qquad (34)$$

Therefore, in the nonlinear behaviour zone the critical parameter is given by the relation in decibels of the 2nd order harmonic (first non-fundamental harmonic) and the fundamental component.

The Taylor series expansion of the output signal around the operation point establishes that [97]:

$$\mathrm{U(I)} = \sum_{\mathrm{k=0}}^{+\infty} \frac{1}{\mathrm{k!}} \cdot \left.\frac{\mathrm{d^k U}}{\mathrm{dI^k}}\right|_{\mathrm{I_{DC}}} \cdot [\mathrm{I} - \mathrm{I_{DC}}]^\mathrm{k} \qquad (35)$$

Introducing the expression of the perturbation signal given by equation expression (9), in equation (35):

$$\mathrm{U(t)} = \sum_{\mathrm{k=0}}^{+\infty} \frac{1}{\mathrm{k!}} \cdot \left.\frac{\mathrm{d^k U}}{\mathrm{dI^k}}\right|_{\mathrm{I_{DC}}} \cdot [\Delta \mathrm{I} \cdot \sin(\omega \cdot \mathrm{t})]^\mathrm{k} \qquad (36)$$

Combining Euler's formula, Newton's binomial theorem and De Moivre's formula [97] the following expression is obtained for the k-th power of a sine function:

$$\sin^{k}(\theta) = \begin{cases} \dfrac{2}{2^{k}} \cdot \displaystyle\sum_{i=0}^{\frac{k-1}{2}} (-1)^{\frac{k-1}{2}-i} \cdot \binom{k}{i} \cdot \sin[(k-2i)\cdot\theta] & k \text{ odd} \\ \dfrac{1}{2^{k}} \cdot \binom{k}{\frac{k}{2}} + \dfrac{2}{2^{k}} \cdot \displaystyle\sum_{i=0}^{\frac{k}{2}-1} (-1)^{\frac{k}{2}-i} \cdot \binom{k}{i} \cdot \cos[(k-2i)\cdot\theta] & k \text{ even} \end{cases} \quad (37)$$

where $\binom{k}{i}$ denotes the binomial coefficients. Using equation (37) in equation (36), and identifying the terms associated to the fundamental component and to the second order harmonic:

$$\Delta U_{1} = \sum_{\substack{k=1 \\ \text{odd}}}^{+\infty} \left.\frac{d^{k}U}{dI^{k}}\right|_{I_{DC}} \cdot \frac{\Delta I^{k}}{k!} \cdot \frac{2}{2^{k}} \cdot \binom{k}{\frac{k-1}{2}} \quad (38)$$

$$\Delta U_{2} = \sum_{\substack{k=2 \\ \text{even}}}^{+\infty} \left.\frac{d^{k}U}{dI^{k}}\right|_{I_{DC}} \cdot \frac{\Delta I^{k}}{k!} \cdot \frac{2}{2^{k}} \cdot \binom{k}{\frac{k}{2}-1} \quad (39)$$

Introducing these expressions in equation (34), the following expression is obtained for the critical parameter:

$$\wp U_{c} = 20 \cdot \log_{10}\left(\frac{\sum_{\substack{k=2 \\ \text{even}}}^{+\infty} \left.\frac{d^{k}U}{dI^{k}}\right|_{I_{DC}} \cdot \frac{\Delta I^{k}}{k!} \cdot \frac{2}{2^{k}} \cdot \binom{k}{\frac{k}{2}-1}}{\sum_{\substack{k=1 \\ \text{odd}}}^{+\infty} \left.\frac{d^{k}U}{dI^{k}}\right|_{I_{DC}} \cdot \frac{\Delta I^{k}}{k!} \cdot \frac{2}{2^{k}} \cdot \binom{k}{\frac{k-1}{2}}} \right) \quad (40)$$

Equation (40) is valid for any general electrochemical system: the nature of the system will define the derivative terms of the expression. As it was defined in the introduction section, this work focuses of Tafelian systems. The U-I relation in this kind of system establishes that [98]:

$$U(I) = a - b \cdot \ln(|I|) \quad (41)$$

Where a and b are the Tafel constants of the system. a stands for the Tafel's ordinate; and b denotes the Tafel's slope. Using the general derivation properties [97]:

$$\left.\frac{d^k U}{dI^k}\right|_{I_{DC}} = \frac{(-1)^k \cdot b \cdot (k-1)!}{|I_{DC}|^k} \quad \forall k \epsilon \mathbb{N} \tag{42}$$

Introducing expression (42) in (40) and simplifying, the following expression is obtained:

$$\wp U_c = 20 \cdot \log_{10}\left(\frac{S}{T}\right) \tag{43}$$

Where S and T are the following series:

$$S = \sum_{k=1}^{+\infty} s_k = \sum_{k=1}^{+\infty} \frac{(2k-1)!}{|I_{DC}|^{2k}} \cdot \frac{\Delta I^{2k}}{(2k)!} \cdot \frac{1}{2^{2k-1}} \cdot \binom{2k}{k-1} \tag{44}$$

$$T = \sum_{k=1}^{+\infty} t_k = \sum_{k=1}^{+\infty} \frac{(2k-2)!}{|I_{DC}|^{(2k-1)}} \cdot \frac{\Delta I^{(2k-1)}}{(2k-1)!} \cdot \frac{1}{2^{(2k-2)}} \cdot \binom{2k-1}{k-1} \tag{45}$$

Since $\Delta I > 0$, S and T are also positive; and therefore equation 43 is well defined. By introducing the binomial term general expression and simplifying:

$$s_k = 2 \cdot \left[\frac{\Delta I}{2 \cdot |I_{DC}|}\right]^{2k} \cdot \frac{(2k-1)!}{(k-1)! \cdot (k+1)!} \tag{46}$$

$$t_k = 2 \cdot \left[\frac{\Delta I}{2 \cdot |I_{DC}|}\right]^{2k-1} \cdot \frac{(2k-2)!}{(k-1)! \cdot k!} \tag{47}$$

The critical parameter $\wp U_c$ is a parameter of a real system: therefore it has to be finite. Equation (43) only fulfils the finiteness condition if both series (S and T) are convergent. Table 2 gives the results of the convergence study of both series, in which 3 different cases were considered: $\Delta I < |I_{DC}|$, $\Delta I = |I_{DC}|$, and $\Delta I > |I_{DC}|$. The convergence criteria used in this work were: the necessary condition for series convergence [97], NCCS; D'Alembert's criterion [97], RT; and the 2nd ratio test [99], 2RT. As it can be seen in table 2, both series converge for $\Delta I \leq |I_{DC}|$, and therefore, equation (43) fulfils the finiteness condition in this case. On the contrary, both series diverge for $\Delta I > |I_{DC}|$. However, this case has no physical meaning: applying a perturbation amplitude larger than the DC current would reverse the polarity of the electrode in some parts of the EIS measurement cycle; and obviously, this has to be avoided in order to obtain representative EIS measurements. Consequently, from the 3 considered cases only two have physical meaning in the modelled situation; and in

both of them the series converge, and therefore, expression (43) is well defined. Using WolframAlpha® the series are summed for the case $\Delta I \leq |I_{DC}|$:

$$S = \frac{-\Delta I^2 + 2 \cdot |I_{DC}|^2 - 2 \cdot |I_{DC}|^2 \cdot \sqrt{\frac{|I_{DC}|^2 - \Delta I^2}{|I_{DC}|^2}}}{\Delta I^2} \quad (48)$$

$$T = \frac{2 \cdot |I_{DC}| \cdot \left(1 - \sqrt{\frac{|I_{DC}|^2 - \Delta I^2}{|I_{DC}|^2}}\right)}{\Delta I} \quad (49)$$

Introducing these expressions in equation (43) and simplifying the obtained expression, the following expression for the critical parameter is obtained:

$$\wp U_c = 20 \cdot \log_{10}\left(\frac{|I_{DC}| \cdot \left(1 - \sqrt{1 - \frac{\Delta I^2}{|I_{DC}|^2}}\right)}{2 \cdot \Delta I}\right) \quad (50)$$

Expression (50) is defined mathematically for $\Delta I \in]0; |I_{DC}|]$. This definition domain is consistent with the physical background of the modelled situation: On the one hand, the perturbation amplitude is a nonzero positive quantity; on the other hand, as explained previously, the perturbation amplitude has to be smaller or equal to the DC current in order to guarantee that the electrode works as the cathodic electrode of the system during the whole EIS measurement.

As explained in section 3, the DC current at which the system was operated was $-10\ mA$. Particularizing expression (50) to this work's particular case:

$$\wp U_c = 20 \cdot \log_{10}\left(\frac{10 - \sqrt{100 - \Delta I^2}}{2 \cdot \Delta I}\right) \quad (51)$$

Where ΔI is expressed in mA. Figure 9 shows the superposition of the theoretical model (given by equation (51)) with the nonlinear behaviour zone of the experimental $\wp U_c$ curve, presented in section 4.2. It can be observed that the theoretical model fits perfectly the experimental $\wp U_c$ curve in the nonlinear behaviour zone: the associated determination coefficient being of 99.72%. Therefore, it can be deduced that the proposed theoretical model actually explains the experimental shape of the $\wp U_c$ curve in the nonlinear behaviour zone.

5.4. Transitions

As it was identified in figure 6, two frequencies are relevant from the critical parameter curve's point of view: the critical frequency of the linear behaviour zone (25 Hz) and the critical frequency of the nonlinear behaviour zone (5 mHz). Figures 10 and 11 present the $\wp U$ versus perturbation amplitude curves for each one of these two frequencies.

On the one hand, in figure 10 it can be observed that the $\wp U$ curve for $f = 25\ Hz$ shows only one trend: it decreases with the perturbation amplitude in the whole amplitude range. Therefore, the $\wp U$ curve for $f = 25\ Hz$ consists only of a linear behaviour zone: no nonlinear effects are observed for this frequency. This can be due to two factors: the 25 Hz frequency may be above the threshold frequency of the system, and therefore, no nonlinear effects would be generated at this frequency even for very large perturbation amplitudes; or the noise at this frequency may be so high that it would completely mask the nonlinear effects for all the perturbation amplitudes. The $\wp U$ curve for $f = 25\ Hz$ was fitted to the linear behaviour zone model given by equation (21), and the obtained fit is represented in figure 10. The obtained fitted model corresponds with the linear model for $f = 25\ Hz$. As it can be observed in the figure, the linear model for $f = 25\ Hz$ accurately represents the corresponding experimental data. Therefore, since no nonlinear effects are observed for $f = 25\ Hz$, the $25\ Hz$ $\wp U$ curve is directly given by the linear model for $f = 25\ Hz$, $\wp U_{\text{linear}}(f_{c\_linear})$:

$$\wp U(f_{c\_linear}) = \wp U_{\text{linear}}(f_{c\_linear}) \qquad (52)$$

On the other hand, in figure 11 it can be observed that the $\wp U$ curve for $f = 5\ mHz$ displays the two-trend-shape. As it has been already explained in previous sections, this two-trend-shape is related to a change of dominance from noise to nonlinear effects. The decreasing part of the $\wp U$ curve for $f = 5\ mHz$ was fitted to the linear behaviour zone model given by equation (21), and the obtained fit is represented in figure 11. In the same graph the theoretical model for nonlinear effects is superimposed. As it can be seen, for low perturbation amplitudes, the linear component (related to noise) is above the nonlinear one: thus, for low perturbation amplitudes, noise dominates over nonlinear effects. On the contrary, for high perturbation amplitudes, the noise related component is below the nonlinear effects related component: therefore, for high perturbation amplitudes, nonlinear effects dominate over noise. According to the definition of parameter $\wp U$ introduced in section 2 and applying the properties of the maximum function, the following

expression can be deduced for the $\wp U$ parameter at the critical frequency of the nonlinear behaviour zone:

$$\wp U\left(f_{c\_nonlinear}\right) = max\left\{\wp U_{\text{linear}}\left(f_{c\_nonlinear}\right); \wp U_{\text{nonlinear}}\right\} \qquad (53)$$

where $\wp U_{\text{linear}}\left(f_{c\_nonlinear}\right)$ denotes the linear model for $f = 5\ mHz$; and $\wp U_{\text{nonlinear}}$ stands for the theoretical nonlinear model given by equation (51). According to this expression, the $\wp U$ curve for $f = 5\ mHz$ corresponds with the linear model for $f = 5\ mHz$ for low perturbation amplitudes (for which noise is the dominant effect). Once the nonlinear effects overcome noise (when the nonlinear model passes above the linear model), the $\wp U$ curve for $f = 5\ mHz$ is given by the nonlinear theoretical model. This is consistent with the $5\ mHz$ experimental data, as it can be seen in figure 11. The point where the nonlinear model intersects the linear model is the linear/nonlinear transition point for $f = 5\ mHz$. It has also been identified on the figure.

Comparing the obtained linear models for $f = 25\ Hz$ and $f = 5\ mHz$, it can be observed that the effective noise parameter of the linear behaviour zone, c_2, is larger in the $25\ Hz$ case. Using the values of c_2 obtained from the fitting of the linear model to the experimental data, the impedance modulus at the corresponding frequency and expression (23), the noise characterization parameter, $\Delta \mathrm{U}_{\mathrm{noise}}$, was calculated for both frequencies. The calculation results are given in table 3. From the obtained results, it can be deduced that the noise level when the EIS measurement is performed at $25\ Hz$ is larger than the noise level of the measurement at $5\ mHz$. Moreover, the impedance modulus of the system at $25\ Hz$ is lower than the impedance modulus of the system at $5\ mHz$. The combination of these two facts (higher noise level and lower impedance modulus) causes the $25\ Hz$ measurement to be more affected by noise than the $5\ mHz$ one, which is the meaning of a higher c_2 parameter value. Consequently, the $\wp U$ curve for $f = 25\ Hz$ is above the linear behaviour zone of the $\wp U$ curve for $f = 5\ mHz$. This can clearly be observed in figure 12.

As it can be seen in figure 12, for very small perturbation amplitudes, the noise is dominant in both frequencies: the system is in the linear behaviour zone for both frequencies. Since the $25\ Hz$ measurement is more affected by noise than the $5\ mHz$ one (it has a higher elective noise parameter, c_2), the critical frequency for low amplitudes is $25\ Hz$. When the perturbation amplitude is increased, both $\wp U$ curves decrease due to the improvement of the signal-to-noise ratio for both frequencies. However, there is a perturbation amplitude at which the nonlinear effects at $5\ mHz$ overcome the noise at that frequency. As it was explained before, this is the linear/nonlinear transition point for $f = 5\ mHz$. Since the noise effect on the $25\ Hz$

measurement is higher than the noise effect on the $5\,mHz$, in the $5\,mHz$ linear/nonlinear transition point the nonlinear effects overcome the $5\,mHz$ noise, but do not overcome the $25\,Hz$ noise. Consequently, the critical frequency is still $25\,Hz$. If the amplitude is increased further: the $25\,Hz$ $\wp U$ curve continues to decrease due to the improvement of the signal-to-noise ratio (no nonlinear effects are observable at $25\,Hz$); and the $5\,mHz$ $\wp U$ curve increases due to an increase in nonlinearity (after the linear/nonlinear transition point the system behaves significantly nonlinearly for $5\,mHz$). If the perturbation amplitude continues to be increased, the critical amplitude is reached: the nonlinear effects at $5\,mHz$ increase so much that they overcome the $25\,Hz$ noise level. At this point there is a critical frequency change: the critical frequency changes from $25\,Hz$ to $5\,mHz$.

According to the definition of the critical parameter $\wp U_{\mathrm{c}}$ introduced in section 2 and applying the properties of the maximum function, the following expression can be deduced for the $\wp U_{\mathrm{c}}$ parameter:

$$\wp U_{\mathrm{c}} = max\{\wp U(f_{c\_linear}); \wp U(f_{c\_nonlinear})\} \qquad (54)$$

According to this expression, the critical parameter curve is given by the highest $\wp U$ curve. Consequently, for low amplitudes the $\wp U_{\mathrm{c}}$ curve corresponds with the $25\,Hz$ $\wp U$ curve; and after the critical frequency change (at the critical amplitude), the $\wp U_{\mathrm{c}}$ curve corresponds with the $5\,mHz$ $\wp U$ curve. This can clearly be seen in figure 12.

5.5. Critical perturbation amplitude

As introduced in section 5.1, the critical amplitude is the perturbation amplitude at which nonlinear effects overcome noise. As seen in the previous subsection, this occurs at the critical frequency change point; which in turn corresponds with the intersection of the linear model for the linear behaviour zone frequency with the nonlinear model. Combining the intersection condition with the expressions of the linear model for the linear behaviour zone frequency, given by equation (24); and of the nonlinear model, given by equation (50); the following expression is obtained:

$$20 \cdot \log_{10}\left(\frac{1}{\Delta \mathrm{I_c}}\right) + c_2(f_{c\_linear}) = 20 \cdot \log_{10}\left(\frac{|\mathrm{I_{DC}}| \cdot \left(1 - \sqrt{1 - \frac{\Delta \mathrm{I_c}^2}{|\mathrm{I_{DC}}|^2}}\right)}{2 \cdot \Delta \mathrm{I_c}}\right) \qquad (55)$$

Solving for the critical perturbation amplitude the following expression is obtained:

$$\Delta I_c = |I_{DC}| \cdot \sqrt{1 - \left(1 - \frac{2 \cdot 10^{\frac{c_2(f_{c\_linear})}{20}}}{|I_{DC}|}\right)^2} \qquad (56)$$

It should be observed that even if mathematically two solutions are valid ($\pm$ the given solution); the negative one has not been considered in this work since it has no physical meaning (perturbation amplitudes are positive values). Moreover, from the mathematical solving process the following condition arises:

$$c_2(f_{c\_linear}) \leq 20 \cdot \log_{10}\left(\frac{|I_{DC}|}{2}\right) \qquad (57)$$

In order to be able to apply equation (56) to calculate the critical amplitude, parameter c_2 must fulfil condition (57). Though this condition arises from a mathematical reasoning, it has a clear physical meaning that will be discussed in detail in section 6.

Particularizing equations (56) and (57) to the case presented in this work, $I_{DC} = -10\ mA$, the following expressions are obtained:

$$\Delta I_c = \sqrt{100 - \left(10 - 2 \cdot 10^{\frac{c_2(f_{c\_linear})}{20}}\right)^2} \qquad (58)$$

$$c_2(f_{c\_linear}) \leq 20 \cdot \log_{10}(5) \qquad (59)$$

As it can be seen in figure 10, in the case of the studied system: $c_2(f_{c\_linear}) = -20.0\ dB$. Note that this corresponds with the value obtained from fitting the whole $25\ Hz$ $\wp U$ curve (figure 10). It is advisable to use this value instead of the value obtained from fitting the linear behaviour zone of the critical parameter curve (figure 8); since it is more accurate because it takes into account a larger number of points. In this case, $-20.0\ dB < 20 \cdot \log_{10}(5)$; and therefore expression (58) can be used to determine the critical amplitude, obtaining a result of $\Delta I_c \approx 1.99\ \mathrm{mA}$. This result is consistent with the critical amplitude estimated from the experimental data in section 4.2.

6. Discussion

As discussed in section 5.5, the critical perturbation amplitude is given by the intersection of the linear behaviour zone curve and the nonlinear behaviour zone curve. Figure 13 represents the nonlinear behaviour model, obtained in section 5.3; and the linear behaviour model, obtained in section 5.2, for different critical effective noise parameter values, $c_2\left(f_{c\_linear}\right)$. All the curves represented in this figure are associated to a DC current of $|\mathrm{I_{DC}}| = 10\ \mathrm{mA}$. The intersection points of the linear behaviour zone model with the linear model associated to each $c_2\left(f_{c\_linear}\right)$ value are identified on the figure. As it can be observed, an increase in the effective noise parameter of the linear behaviour zone displaces the intersection point to higher critical perturbation amplitudes. This is due to the fact that a higher $c_2\left(f_{c\_linear}\right)$ value implies that the net effect of the noise in the linear zone critical frequency is higher; and therefore, higher nonlinear effects can be generated before the nonlinear effects overcome the noise. This leads to a higher critical perturbation amplitude. This observation is consistent with expression (58).

A limit case is identified in figure 13: in this limit case, the intersection point occurs at the maximum perturbation amplitude. This limit case is the case in which the effective noise level in the linear behaviour zone is so high that it is only overcome by the nonlinear effects at the maximum perturbation amplitude. In this limit case, the critical parameter curve only displays the linear behaviour zone: the effective noise is so high that nonlinear effects are not observable even at the maximum perturbation amplitude. For $c_2\left(f_{c\_linear}\right)$ values larger than the limit case $c_2\left(f_{c\_linear}\right)$ value, the nonlinear effects do not overcome the noise even at the maximum perturbation amplitude. Therefore, the limit case $c_2\left(f_{c\_linear}\right)$ value defines the effective noise parameter limit between the situation where the noise can be overcome by nonlinear effects at a certain critical amplitude (two-zone critical parameter curve); and the situation where nonlinear effects do not overcome noise even for the maximum perturbation amplitude (one-zone critical parameter curve). This limit case is associated with condition (57), which arose from the mathematical solving process described in section 5.5. Consequently, the limit case $c_2\left(f_{c\_linear}\right)$ value is given by the following expression:

$$c_{lim} = 20 \cdot \log_{10}\left(\frac{|\mathrm{I_{DC}}|}{2}\right) \qquad (60)$$

where c_{lim} stands for the limit effective noise parameter: above this effective noise level, nonlinear effects are not observable even at the maximum perturbation amplitude on account of the high noise level that masks the nonlinear effects. This parameter defines the limit between the two-zone critical parameter curve (linear

behaviour zone and nonlinear behaviour zone) and the one-zone critical parameter curve (only the linear behaviour zone).

Figure 14 represents the critical perturbation amplitude versus the effective noise parameter, for different DC currents. It is the graphical representation of equation (56). The dashed line represents the limit effective noise parameter, given by equation (60). It can be observed that for $c_2\left(f_{c\_linear}\right) < c_{lim}$, an increase in the effective noise parameter leads to a higher critical perturbation amplitude. But for effective noise levels above c_{lim} the nonlinear effects do not appear even for the maximum perturbation amplitude: therefore, in this case, the critical amplitude corresponds to the maximum perturbation itself. For this reason, saturation is observed in the curves after passing the dashed line.

Moreover, from equation (56) the following limit can be deduced:

$$\lim_{c_2(f_{c\_linear})\to-\infty} \Delta \mathrm{I_c} = 0 \qquad (61)$$

This is consistent with the curves shown in figure 14. Therefore, an extremely low effective noise level leads to null critical perturbation amplitude. This has a very important conceptual implication: a nonlinear system is always nonlinear; noise masks the non fundamental harmonics generated by nonlinear effects, and thus, noise is responsible for the quasi-linear behaviour of the system. In the theoretical case in which no noise would be present in the system $\left(c_2\left(f_{c\_linear}\right) \to -\infty\right)$, even very small perturbation amplitudes would generate observable nonlinear effects: and therefore the critical amplitude would be 0. Consequently, the definition of quasi-linear behaviour is linked to the noise level: a system behaves quasi-linearly when the nonlinear effects are masked by the noise. In other words, when nonlinear effects are negligible (in comparison with the noise).

7. Conclusions

In this work, a harmonic analysis based method for linearity assessment and noise quantification in EIS measurements has been validated successfully, both from an experimental point of view and from a theoretical point of view, for Tafelian systems. The main advantage of this method over the methods commonly used for linearity assessment (i.e. AC plots and Lissajous plots) is that it is a quantitative method that allows to accurately quantify the signal-to-noise ratio and the magnitude of the nonlinear effects. Furthermore, this method is able to distinguish the nonlinear effects from the noise. This allows, for instance, to compare the nonlinearity of two different systems. This constitutes a major advantage of the presented method over other harmonic analysis methods available in literature.

On the one hand, the presented method is able to determine the critical perturbation amplitude which delimits the zone where the linearity hypothesis can be accepted and where it cannot be accepted. This may be used for perturbation amplitude optimization. On the other hand, the presented method is able to determine the threshold frequency of the system, above which no significant nonlinear effects appear even for high perturbation amplitudes. This information can be used to determine which part of the EIS spectrum of the system is sensitive to nonlinear effects, and which one is not. Finally, the presented method allows quantifying and characterising noise. It may even be used in order to track the sources of noise in the system (i.e. electric coupling of the system with the grid). Consequently, the method presented in this work has a clear utility in linearity assessment of electrochemical systems; and in noise quantification and characterization. However it does not replace the impedance measurements themselves: once the linearity condition has been validated and the noise has been quantified, the impedance measurements have to be analysed as usual.

It should be noted that this linearity assessment method does not require the knowledge of the underlying impedance model of the system (in this work, the impedance model has not even been mentioned!). This is a great advantage of the presented linearity assessment method: it can be applied to any tafelian system regardless of its underlying mechanism. It can even be applied to systems for which no prior knowledge on their impedance model is available.

8. Nomenclature

Latin letters

a	Tafel's ordinate (V)
b	Tafel's slope (V/dec)
c_1	Constant parameter of the linear behaviour zone model (dB)
c_2	Effective noise parameter of the linear behaviour zone model (dB)
c_{lim}	Limit effective noise parameter (dB)
$\mathcal{F}$	Fourier transform operator
f	Frequency (Hz)
f_c	Critical frequency (Hz)
f_{c_linear}	Critical frequency of the linear behaviour zone (Hz)
$f_{c\_nonlinear}$	Critical frequency of the nonlinear behaviour zone (Hz)
I	Current in the time domain (A)
$\hat{I}$	Current in the frequency domain (A)
I_{DC}	Polarization current (A)
N_f	Number of measured frequencies
R^2	Determination coefficient
t	Time domain independent variable (s)
U	Potential in the time domain (V)
$\widehat{U}$	Potential in the frequency domain (V)
Z	Complex impedance (Ω)
$\|Z\|$	Impedance modulus (Ω)
Z'	Real part of complex impedance (Ω)
Z''	Imaginary part of complex impedance (Ω)

Greek letters

ΔI	Galvanostatic perturbation amplitude (A)
ΔI_c	Critical galvanostatic perturbation amplitude (A)
ΔU_k	k-th component of the output signal generated by the response of the system (V)
ΔU_{nk}	k-th component of the output signal associated to noise (V)
ϑ	Frequency domain independent variable (Hz)
$\wp I$	Ratio between the most important non-fundamental harmonic of the current signal, and its fundamental component (dB)
$\wp I_c$	Critical parameter for the current signal (dB)
$\wp U$	Ratio between the most important non-fundamental harmonic of the voltage signal, and its fundamental component (dB)
$\wp U_c$	Critical parameter for the voltage signal (dB)

φ_k	Phase lag of the k-th component of the output signal (rad)
ω	Angular frequency $(rad \cdot s^{-1})$

9. Acknowledgments

The authors are very grateful to the Generalitat Valenciana for its economic support in form of Vali+d grant (Ref: ACIF-2013-268).

10. Bibliography

[1] M.E. Orazem, B. Tribollet, Electrochemical impedance spectroscopy, John Wiley & Sons, New Jersey, 2008.
[2] A. Lasia, Electrochemical impedance spectroscopy and its applications, Springer, London, 2014.
[3] E. Barsoukov, J.R. Macdonald, Impedance spectroscopy. Theory, experiment and applications, John Wiley & Sons, New Jersey, 2005.
[4] D.D. Macdonald, Reflections on the history of electrochemical impedance spectroscopy, Electrochim. Acta 51 (2006) 1376.
[5] F. Ciucci, C. Chen, Analysis of electrochemical impedance spectroscopy data using the distributionof relaxation times: A bayesian and hierchical Bayesian approach, Electrochim. Acta 167 (2015) 439.
[6] J. Li, N. Zhang, K. Sun, Z. Wu, High thermal stability of three-dimensionally ordered nanp-composite cathodes for solid oxide fuel cells, Electrochim. Acta 187 (2016) 179.
[7] E.C. Shin et al., Deconvolution of four transmission-line-model impedances in Ni-YSZ/YSZ/LSM solid oxide cells and mechanistic insights, Electrochim. Acta 188 (2016) 240.
[8] A. Baricci, A. Casalengo, A simple analytical approach to simulate the electrochemical impedance response of flooded agglomerates in polymer fuel cells, Electrochim. Acta 157 (2015) 324.
[9] N. Nasani, D. Ramasamy, I. Antunes, J. Perez, D.P. Fagg, Electrochemical behaviour of Ni-BZO and Ni-BZY cermet anodes for protonic ceramic fuel cells (PCFCs) - A comparative study, Electrochim. Acta 154 (2015) 387.
[10] X. Li et al., Enhanced activity and durability of platinum anode catalyst by the modification of cobalt phosphide for direct methanol fuel cells, Electrochim. Acta 185 (2015) 178.
[11] H. Sumi, T. Ohshiro, M. Nakayama, T. Suzuki, Y. Fujishiro, Prevention of reaction between (Ba,Sr)(Co,Fe)O3 cathodes and yttria-stabilized Zirconia electrolytes for intermediate-temperature solid oxide fuel cells, Electrochim. Acta 184 (2015) 403.
[12] S.K. Kamaraj, S.M. Romano, V.C Moreno, H.M. Poggi-Varaldo, O. Solorza-Feria, Use of novel reinforced cation exchange membranes for microbial fuel cells, Electrochim. Acta 176 (2015) 555.
[13] Z. Yang, S. Wang, K. Dong, Y. Dai, X. Lei, Electrochemical characterization of sulfur with low depth of charge/discharge in lithium sulfur batteries, Electrochim. Acta 187 (2016) 629.
[14] Y. Yan, L. Ben, Y. Zhan, X. Huang, Nano-Sn embedded in expanded graphite as anode for lithium ion batteries with improved low temperature electrochemical performance, Electrochim. Acta 187 (2016) 186.
[15] W. Wu, Y. Liang, H. Ma, Y. Peng, H. Yang, Insights into the conversion behaviour of SiO-C hybrid with pre-treated graphite as anodes for Li-ion batteries, Electrochim. Acta 187 (2016) 473.
[16] H. Wang et al., Biomass derived hierarchical porous carbons as high-performance anodes for sodium-ion batteries, Electrochim. Acta 188 (2016) 103.
[17] A. Ramos, I. Camean, N. Cuesta, C. Antuña, A.B. Garcia, Expanded graphitic materials prepared from micro- and nanometric precursors as anodes for sodium-ion batteries, Electrochim. Acta 187 (2016) 496.

[18] G. Qian et al., Polyimide binder: A facile way to improve safety of lithium ion batteries, Electrochim. Acta 187 (2016) 113.
[19] C. Boissy, B. Ter-Ovanessian, N. Mary, B. Normand, Correlation between predictive and descriptive models to characterize the passive film - Study of pure chromium by electrochemical impedance spectroscopy, Electrochim. Acta 174 (2015) 430.
[20] L. Kavan et al., Boron-doped diamond electrodes: Electrochemical, atomic force microscopy and Raman study towards corrosion-modifications at nanoscale, Electrochim. Acta 179 (2015) 626.
[21] V. Shkirskiy, K. Ogle, A novel coupling of electrochemical impedance spectroscopy with atomic emission spectroelectrochemistry: Application to the open circuit dissolution of Zinc, Electrochim. Acta 168 (2015) 167.
[22] C.A. Badica, P. Chirita, An electrochemical study of the oxidative dissolution of iron monosulfide (FeS) in air-equilibrated solutions, Electrochim. Acta 178 (2015) 786.
[23] K. Sipila, M. Bojinov, W. Mayinger, T. Saario, M. Stanislowski, Effect of chloride and sulfate additions on corrosion of low alloy steel in high-temperature water, Electrochim. Acta 173 (2015) 757.
[24] Z. Feng, G.S. Frankel, Evaluation of coated Al alloy using breakpoint frequency method, Electrochim. Acta 187 (2016) 605.
[25] X. Lu et al., Plasma electrolytic oxidation coatings on Mg alloy with addition of SiO2 particles, Electrochim. Acta 187 (2016) 20.
[26] L. Wang et al., High performance carbon-coated lithium zinc titanate as an anode material for lithium-ion batteries, Electrochim. Acta 188 (2016) 135.
[27] S. Tang et al., Label free electrochemical sensor for Pb2+ based on graphene oxide mediated deposition of silver nanoparticles, Electrochim. Acta 187 (2016) 286.
[28] S. Li, G. Yin, X. Wu, C. Liu, J. Luo, Supramolecular imprinted sensor for carbofuran detection based on a functionalized multiwalled carbon nanotube-supported Pd-Ir composite and methylene blue as catalyst, Electrochim. Acta 188 (2016) 294.
[29] J.P.C Trigueiro, R.L. Lavall, G.G. Silva, Nanocomposites of graphene nanosheets/Multiwalled carbon nanotubes as electrodes for in-plane supercapacitors, Electrochim. Acta 187 (2016) 312.
[30] Y. Zou et al., One-pot synthesis of ternary polypyrrole-prussian blue-grapehene-oxide hybrid composite as electrode material for high-performance supercapacitors, Electrochim. Acta 188 (2016) 126.
[31] H. Fan et al., Thin Co3O4 nanosheet array on 3D porous graphene/nickel foam as a binder-free electrode for high-performance supercapacitors, Electrochim. Acta 188 (2016) 222.

[32] A.V. Kuzmin, E.V. Yurtov, Liquid crystals of Lithium dodecylbenzenesulfonate for electric double layer capacitors, Electrochim. Acta 187 (2016) 98.
[33] T. Jurik et al., Nanostructured gold deposited in gelatin template applied for electrochemical assay of glucose in serum, Electrochim. Acta 188 (2016) 277.
[34] W. Dai et al., Fabrication of Nickel/nanodiamond/boron-doped diamond electrode for non-enzymatic glucose biosensor, Electrochim. Acta 187 (2016) 413.
[35] R.K. Shervedani, M.S. Foroushani, Comparative electrochemical behaviourof proteins: Cytochrome C, Agaricus Bisporus Laccase, and Glucose Oxidase, immobilized onto Gold-Thiol

self-assembled monolayer via electrostatic, covalent and covalent coordinate bond methods, Electrochim. Acta 187 (2016) 646.
[36] G. Congur, E. Eksin, A. Erdem, Impedimetric detection of micro RNA at graphene oxide modified sensors, Electrochim. Acta 172 (2015) 20.
[37] V.W.S. Hung et al., Electrochemical impedance spectroscopy for monitoring caspase-3 activity, Electrochim. Acta 162 (2015) 79.
[38] H. Quan et al., Electrochemical detection of carcinoembryonic antigen based on silver nanocluster/horseradish peroxidase nanocomposite as signal probe, Electrochim. Acta 176 (2015) 893.
[39] R. Wang, J. Di, J. Ma, Z. Ma, Highly sensitive detection of cancer cells by electrochemical impedance spectroscopy, Electrochim. Acta 61 (2012) 179.
[40] W.H. Hassen, V. Duplan, E. Frost, J.J. Dubowski, Quantification of influenza A virus in the presence of extraneous protein using electrochemical impedance spectroscopy, Electrochim. Acta 56 (2011) 8325.
[41] A. Sargent, O.A. Sadik, Monitoring antibody-antigen reactions at conducting polymer-based immunosensors using impedance spectroscopy, Electrochim. Acta 44 (1999) 4667.
[42] M.G. Gray, J.W. Goodman, Fourier Transforms. An introduction for engineers, Springer, New York, 1995.
[43] M. Schonleber, D. Klotz, E. Ivers-Tiffee, A method for improving the robustness of linear Kramers-Kronig validity tests, Electrochim. Acta 131 (2014) 20.
[44] G.S. Popkirov, R.N. Schindler, Optimization of the perturbation signal for electrochemical impedance spectroscopy in the time domain, Rev. Sci. Instrumen. 64 (1993) 3111.
[45] J.E. Garland, C.M. Pettit, D. Roy, Analysis of experimental constraints and variables for time resolved detection of Fourier transform electrochemical impedance spectra, Electrochim. Acta 49 (2004) 2623.
[46] M.E. Orazem, B. Tribollet, An integrated approach to electrochemical impedance spectroscopy, Electrochim. Acta 53 (2008) 7360.
[47] M. Urquidi-Macdonald, S. Real, D.D. Macdonald, Applications of Kramers-Kronig transforms in the analysis of electrochemical impedance data - III. Stability and linearity, Electrochim. Acta 35 (1990) 1559.
[48] D.D. Macdonald, E. Sikora, Characterizing electrochemical systems in the frequency domain, Electrochim. Acta 43 (1997) 87.
[49] C. Hernandez-Jaimes, J. Vazquez-Arenas, J. Vernon-Carter, J. Alvarez-Ramirez, A nonlinear Cole-Cole model for large-amplitude electrochemical impedance spectroscopy, Chem. Eng. Sci. 137 (2015) 1.
[50] N.S. Kaisare, V. Ramani, K. Pushpavanam, S. Ramanathan, An analysis of drifts and nonlinearities in electrochemical impedance spectra, Electrochim. Acta 56 (2011) 7467.
[51] K. Darowicki, The amplitude analysis of impedance spectra, Electrochim. Acta 40 (1995) 439.
[52] S.N. Victoria, S. Ramanathan, Effect of potential drift and ac amplitude on the electrochemical impedance spectra, Electrochim. Acta 56 (2011) 2606.
[53] B. Hirschorn, B. Tribollet, M.E. Orazem, On selection of the perturbation amplitude required to avoid nonlinear effects in impedance measurements, Israel J. Chem. 48 (2008) 133.
[54] M. Kiel, O. Bohlen, D.U. Sauer, Harmonic analysis for identification of nonlinearities in impedance spectroscopy, Electrochim. Acta 53 (2008) 7367.

[55] X.Z. Yuan, C. Song, H. Wang, J. Zhang, Electrochemical impedance spectroscopy in PEM fuel cells. Fundamentals and applications, Springer, London, 2010.
[56] J.J. Giner-Sanz, E.M. Ortega, V. Perez-Herranz, Optimization of the perturbation amplitude for impedance measurements in a commercial PEM fuel cell using total harmonic distortion, Fuel Cells doi10.1002/fuce.201500141.
[57] K. Darowicki, Frequency dispersion of harmonic components of the current of an electrode process, J. Electroanal. Chem. 394 (1995) 81.
[58] K. Darowicki, Linearization in impedance measurements, Electrochim. Acta 42 (1997) 1781.
[59] J. Smulko, K. Darowicki, Nonlinearity of electrochemical noise caused by pitting corrosion, J. Electroanal. Chem. 545 (2003) 59.
[60] J.P Diard, B. Le Gorrec, C. Montella, Theoretical formulation of the odd harmonic test criterion for EIS measurements, J. Electroanal. Chem. 377 (1994) 61.
[61] J.P. Diard, B. Le Gorrec, C. Montella, Impedance measurement errors due to non-linearities - I. Low frequency impedance measurements, Electrochim. Acta 39 (1994) 539.
[62] J.P. Diard, B. Le Gorrec, C. Montella, Deviation from the polarization resistance due to non-linearity. I-Theoretical formulation, J. Electroanal. Chem. 432 (1997) 27.
[63] J.P. Diard, B. Le Gorrec, C. Montella, Deviation of the polarization resistance due to non-linearity - II. Application to electrochemical reactions, J. Electroanal. Chem. 432 (1997) 41.
[64] J.P. Diard, B. Le Gorrec, C. Montella, Deviation of the polarization resistance due to non-linearity - III. Polarization resistance determination from non-linear impedance measurements, J. Electroanal. Chem. 432 (1997) 53.
[65] J.P. Diard, B. Le Gorrec, C. Montella, Non-linear impedance for a two-step electrode reaction with an intermediate adsorbed species, Electrochim. Acta 42 (1997) 1503.
[66] E. Van Gheem et al., Electrochemical impedance spectroscopy in the presence of non-linear distortions and non-stationary behaviour. Part I: Theory and validation, Electrochim. Acta 49 (2004) 4753.
[67] E. Van Gheem et al., Electrochemical impedance spectroscopy in the presence of non-linear distortions and non-stationary behaviour. Part II. Application to crystallographic pitting corrosion of aluminium, Electrochim. Acta 51 (2006) 1443.
[68] W. Lai, Fourier analysis of complex impedance (amplitude and phase) in nonlinear systems: A case study of diodes, Electrochim. Acta 55 (2010) 5511.
[69] G.S Popkirov, R.N. Schindler, Effect of sample nonlinearity on the performance of time domain electrochemical impedance spectroscopy, Electrochim. Acta 40 (1995) 2511.
[70] C. Montella, J.P. Diard, Wolfram Demonstrations Project, 2014, http://demonstrations.wolfram.com/NonlinearImpedanceOfTafelianElectrochemicalSystems/

[71] C. Montella, Combined effects of Tafel kinetics and ohmic potential drop on the nonlinear responses of electrochemical systems to low-frequency sinusoidal perturbation of electrode potential- New approach using the Lambert W-function, J. Electroanal. Chem. 672 (2012) 17.
[72] F. Fasmin, R. Srinivasan, Detection of nonlinearities in electrochemical impedance spectra by Kramers-Kronig transforms, J. Solid State Electr. 19 (2015) 1833.
[73] P. Agarwal, M.E. Orazem, L.H. Garcia-Rubio, Application of measurement models to impedance spectroscopy - III. Evaluation of consistency with the Kramers-Kronig relations, J. Electrochem. Soc. 142 (1995) 4159.

[74] B.A. Boukamp, J.R. Macdonald, Alternatives to Kronig-Kramers transformation and testing, and estimation of distributions, Solid State Ionics 174 (1994) 85.
[75] B.A. Boukamp, A linear Kronig-Kramers transform test for immittance data validation, J. Electrochem. Soc. 142 (1995) 1885.
[76] P. Agarwal, M.E. Orazem, L.H. Garcia-Rubio, Measurement models for electrochemical impedance spectroscopy: I. Demonstration of applicability, J. Electrochem. Soc. 139 (1992) 1917.
[77] P. Agarwal, O.D. Crisalle, M.E. Orazem, L.H. Garcia-Rubio, Application of measurement models to impedance spectroscopy: II. Determination of the stochastic contribution to the error structure, J. Electrochem. Soc. 142 (1995) 4149.
[78] P. Agarwal, M.E. Orazem, L.H. Garcia-Rubio, The influence of error structure on interpretation of impedance spectra, Electrochim. Acta 41 (1996) 1017.
[79] M.E. Orazem, J.M. Esteban, O.C. Moghissi, Practical applications of the Kramers-Kronig relations, Corrosion 47 (1991) 248.
[80] M.E. Orazem, P. Agarwal, C. Deslouis, B. Tribollet, Application of measurement models to electrohydrodynamic impedance spectroscopy, J. Electrochem. Soc. 143 (1996) 948.
[81] M.E. Orazem, P. Shukla, M.A. Membrino, Extension of the measurement model approach for deconvolution of underlying distributions for impedance measurements, Electrochim. Acta 47 (2002) 2027.
[82] M.E. Orazem, A systematic approach toward error structure identification for impedance spectroscopy, J. Electroanal. Chem. 572 (2004) 317.
[83] P.K. Shukla, M.E. Orazem, O.D. Crisalle, Validation of the measurement model concept for error structure identification, Electrochim. Acta 49 (2004) 2881.
[84] B. Hirschorn, M.E. Orazem, On the sensitivity of the Kramers-Kronig relations to nonlinear effects in impedance measurements, J. Electrochem. Soc. 156 (2009) 345.
[85] J.J. Giner-Sanz, E.M. Ortega, V. Perez-Herranz, Montecarlo based quantitative Kramers-Kronig test for PEMFC impedance spectrum validation, Int. J. Hydrogen Energ. 40 (2015) 11279.
[86] J.J. Giner-Sanz, E.M. Ortega, V. Perez-Herranz, Application of a Montecarlo based quantitative Kramers-Kronig test for linearity assessment of EIS measurements, Electrochim. Acta 209 (2016) 254.
[87] R. Pintelon, E. Louarroudi, J. Lataire, Detecting and quantifying the nonlinear and time-variant effects in FRF measurements using periodic excitations, IEEE T. Instrum. Meas. 62 (2013) 3361.
[88] R. Pintelon, E. Louarroudi, J. Lataire, Nonparametric time-variant frequency response function estimates using arbitrary excitations, Automatica 51 (2015) 308.
[89] J.J. Giner-Sanz, E.M. Ortega, V. Perez-Herranz, Total harmonic distortion based method for linearity assessment in electrochemical systems in the context of EIS, Electrochim. Acta 186 (2015) 598.
[90] D. Sundararajan, The discrete Fourier transform. Theory, algorithms and applications, World Scientific, London, 2001.
[91] I. Herraiz-Cardona, Desarrollo de nuevos materiales de electrodo para la obtencion de hidrogeno a partir de la electrolisis alcalina del agua, Valencia, Spain, PhD Thesis, 2012.

[92] I. Herraiz-Cardona, E.M. Ortega, V. Perez-Herranz, Assessment of the roughness factor and the intrinsic catalytic activity for hydrogen evolution reaction on Ni-based electrodeposits, Int. J. Hydrogen Energ. 36 (2011) 9428.
[93] I. Herraiz-Cardona, E.M. Ortega, V. Perez-Herranz, Impedance study of hydrogen evolution on Ni/Zn and Ni-Co/Zn stainless steel based electrodeposits, Electrochim. Acta 56 (2011) 1308.
[94] I. Herraiz-Cardona, E.M. Ortega, L. Vazquez-Gomez, V. Perez-Herranz, Electrochemical characterization of a NiCo/Zn cathode for hydrogen generation, Int. J. Hydrogen Energ. 36 (2011) 11578.
[95] J. Garcia-Anton, A. Igual-Muñoz, J.L. Guiñon, V. Perez-Herranz, Horizontal cell for electro-optical analysis of electrochemical processes, ES patent P-2000002526, October 2000.
[96] J.J. Giner-Sanz, E.M. Ortega, V. Perez-Herranz, Optimization of the electrochemical impedance spectroscopy measurement parameters for PEM fuel cell spectrum determination, Electrochim. Acta 174 (2015) 1290.
[97] I.N. Bronshtein, K.A. Semendyayev, G. Musiol, H. Muehlig, Handbook of Mathematics, Springer, Berlin, 2007.
[98] A.J. Bard, L.R. Faulkner, Electrochemical methods: Fundamentals and applications, John Wiley and Sons, New York, 2001.
[99] A. Sayel, The mth ratio test: New convergence test for series, Am. Math. Mon. 115 (2008) 514.

LIST OF TABLES.

LIST OF FIGURES.

Table 1. EIS measurement parameters

Measurement parameter	**Value**
Integration time	$1.0\ s$
Number of integration cycles	$1\ cycle$
Number of stabilization cycles	$10\ cycles$
Maximum stabilization time	$3.0\ s$
Minimum stabilization cycle fraction	0.00

Table 2. Convergence study results

Series	$\Delta I < \lvert I_{DC} \rvert$		$\Delta I = \lvert I_{DC} \rvert$		$\Delta I > \lvert I_{DC} \rvert$	
	Convergence	Criterion	Convergence	Criterion	Convergence	Criterion
S	Yes	RT	Yes	2RT	No	NCCS
T	Yes	RT	Yes	2RT	No	NCCS

Table 3. Noise characterization parameter calculation

f	$c_2(f)\ (dB)$	|Z(f)| (Ω)	$\Delta U_{noise}(f)\ (V)$
$f_{c\_linear} = 25\ Hz$	−20.0	1.86	0.187
$f_{c\_nonlinear} = 5\ mHz$	−33.1	4.76	0.106

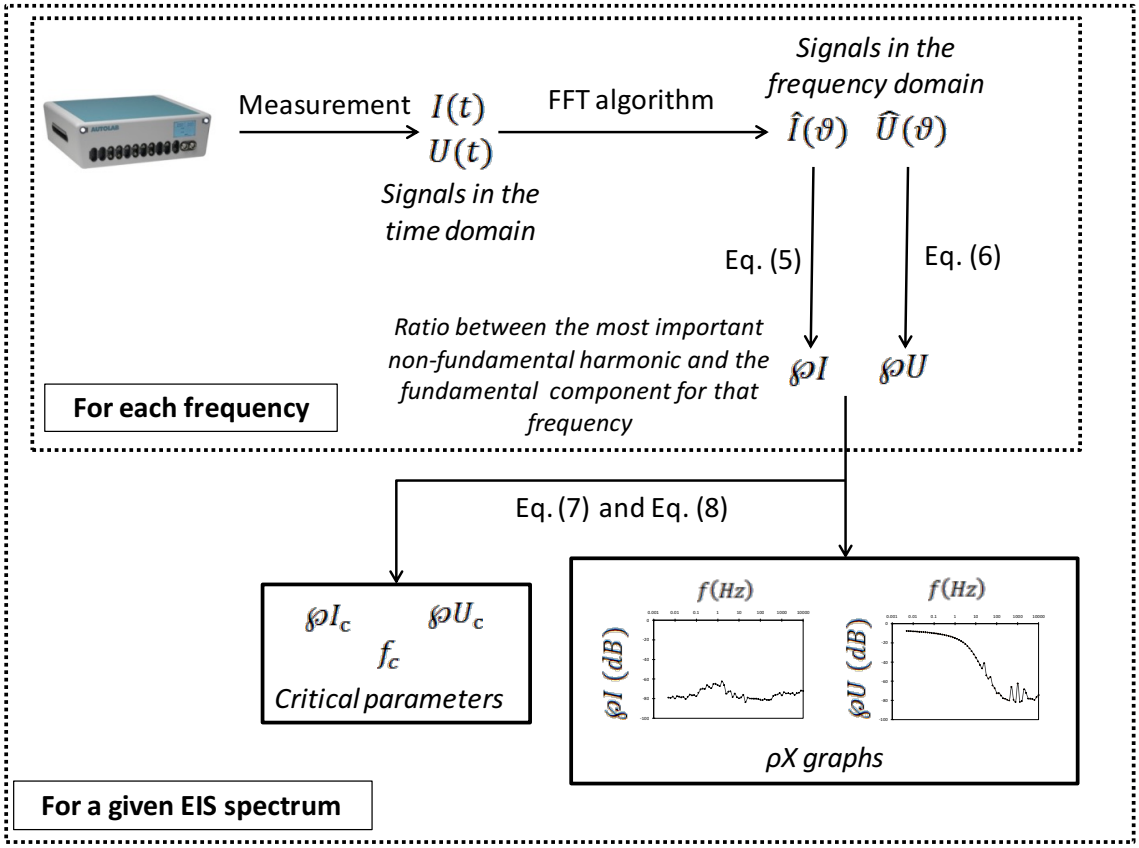

Figure 1. Linearity assessment method outline

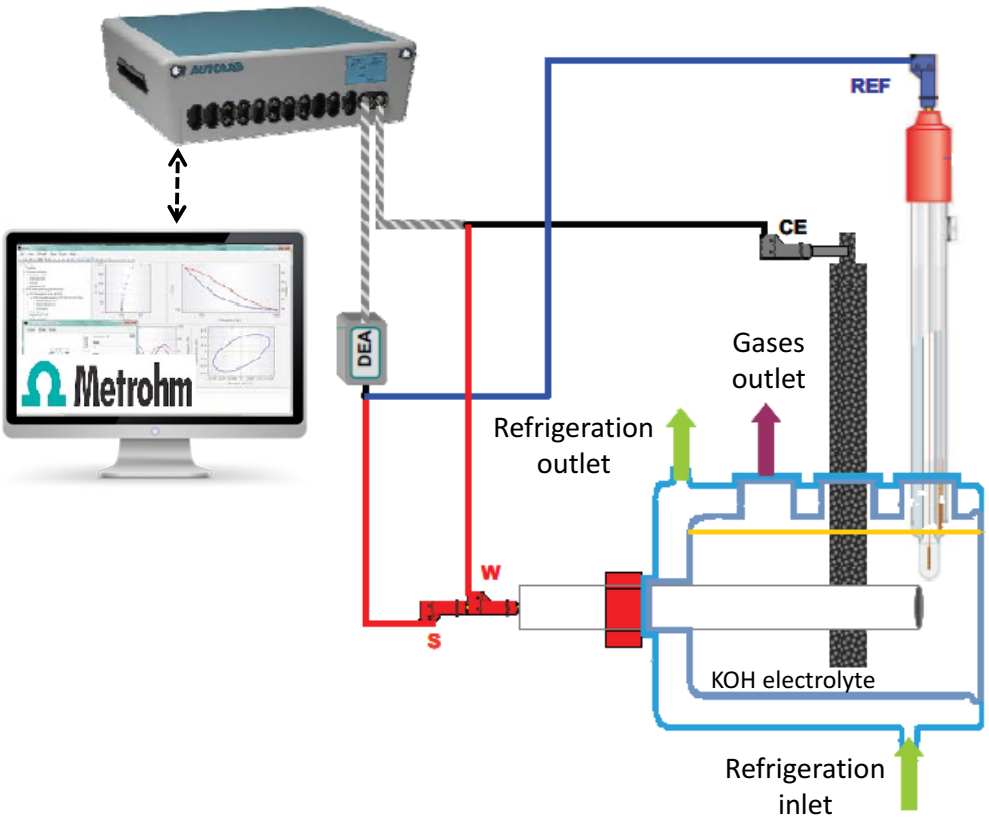

Figure 2. Experimental setup

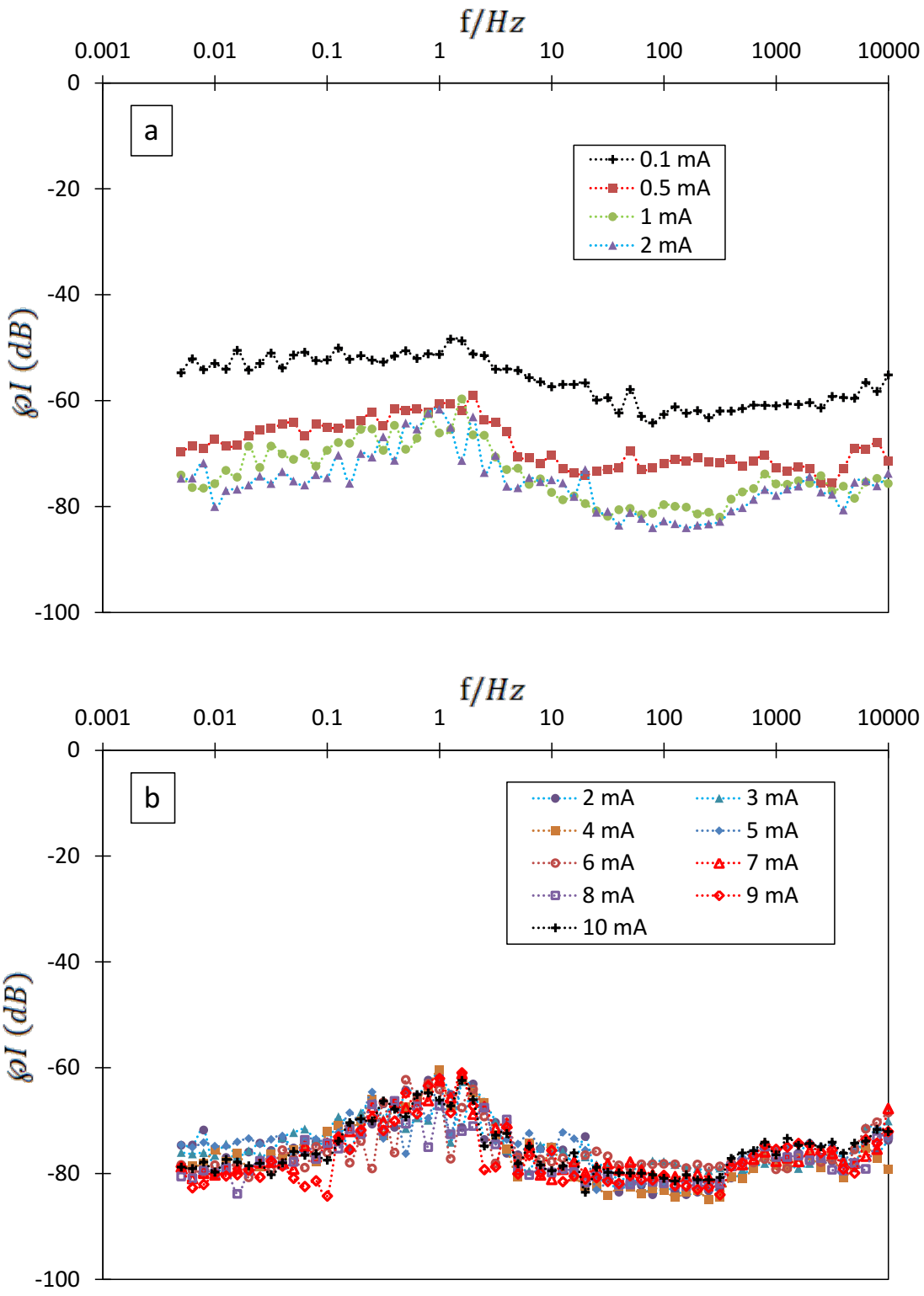

Figure 3. Perturbation signal $\wp I$ curves: Experimentally obtained $\wp I$ ratio for each excitation frequency for low perturbation amplitudes (a) and high perturbation amplitudes (b)

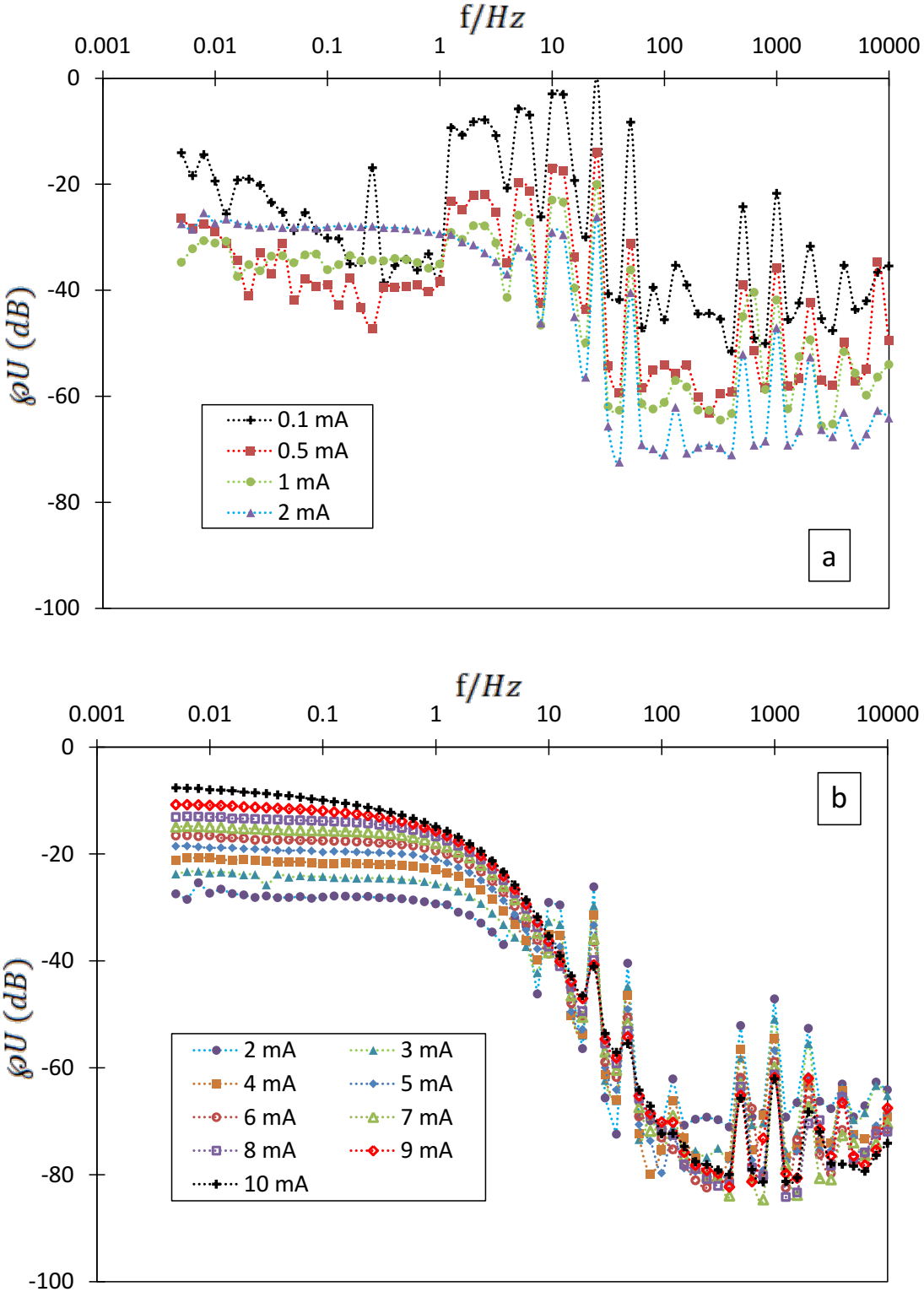

Figure 4. Response signal $\wp U$ curves: Experimentally obtained $\wp U$ ratio for each excitation frequency for low perturbation amplitudes (a) and high perturbation amplitudes (b)

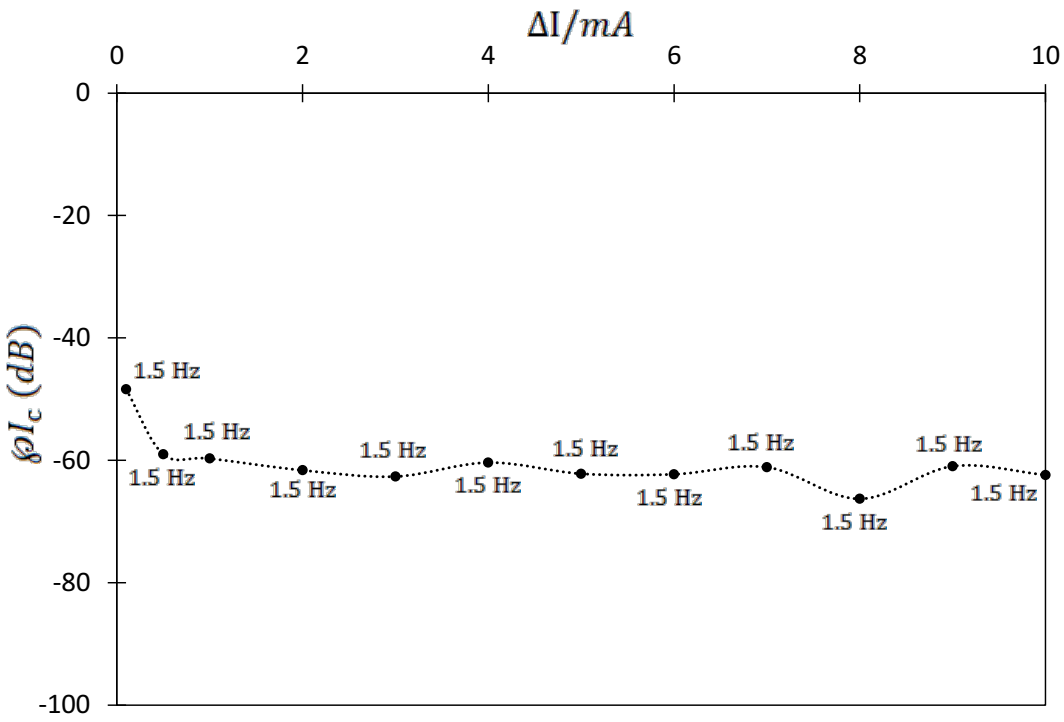

Figure 5. Critical parameter curve for the perturbation signal: experimentally obtained critical ratio and critical frequency for each perturbation amplitude

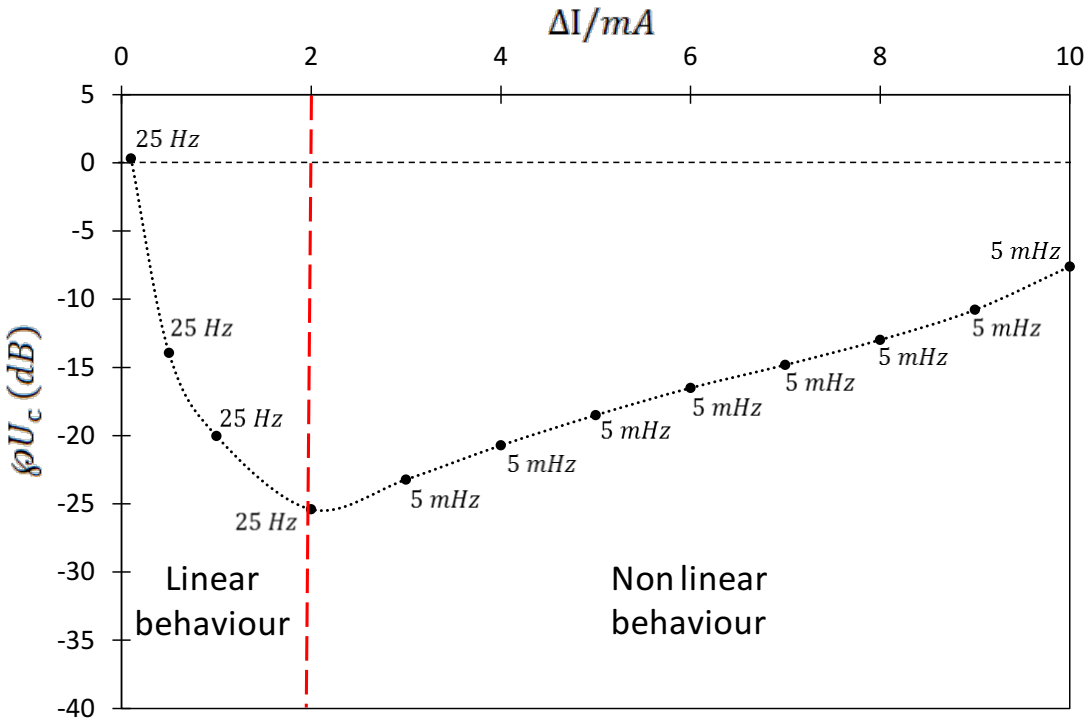

Figure 6. Critical parameter curve for the response signal: experimentally obtained critical ratio and critical frequency for each perturbation amplitude

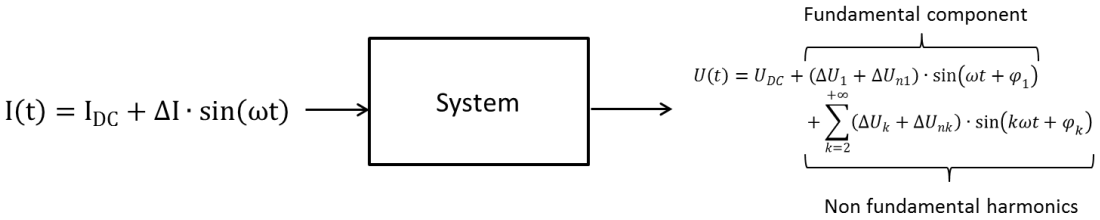

Figure 7. System model

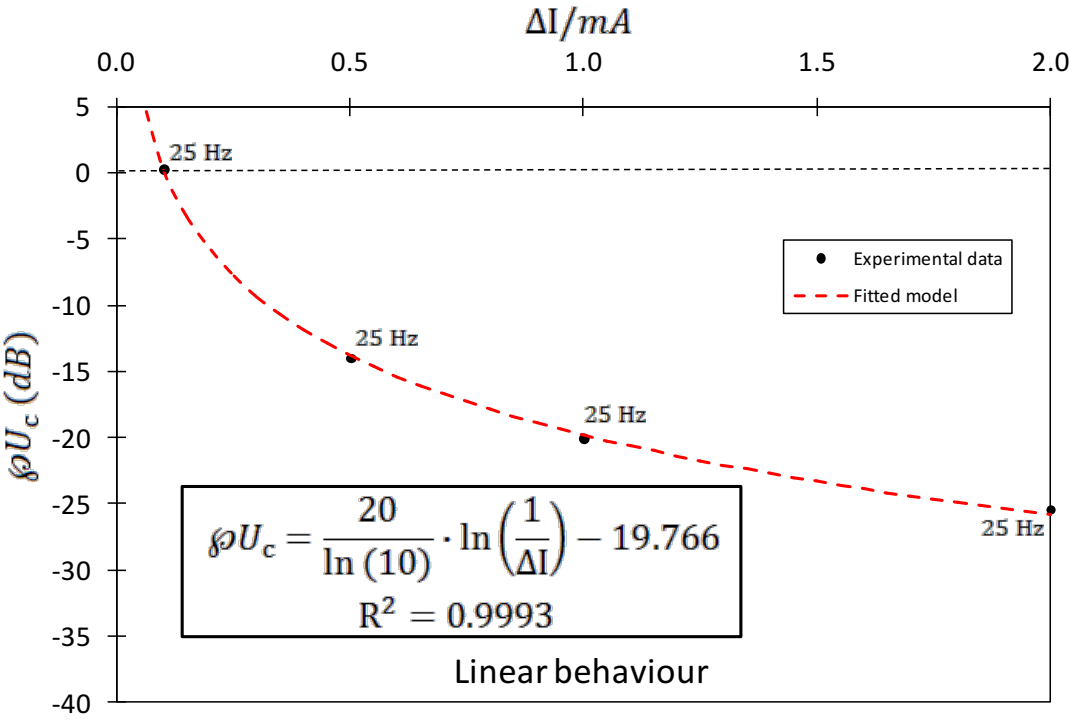

Figure 8. Linear behaviour zone model fitting

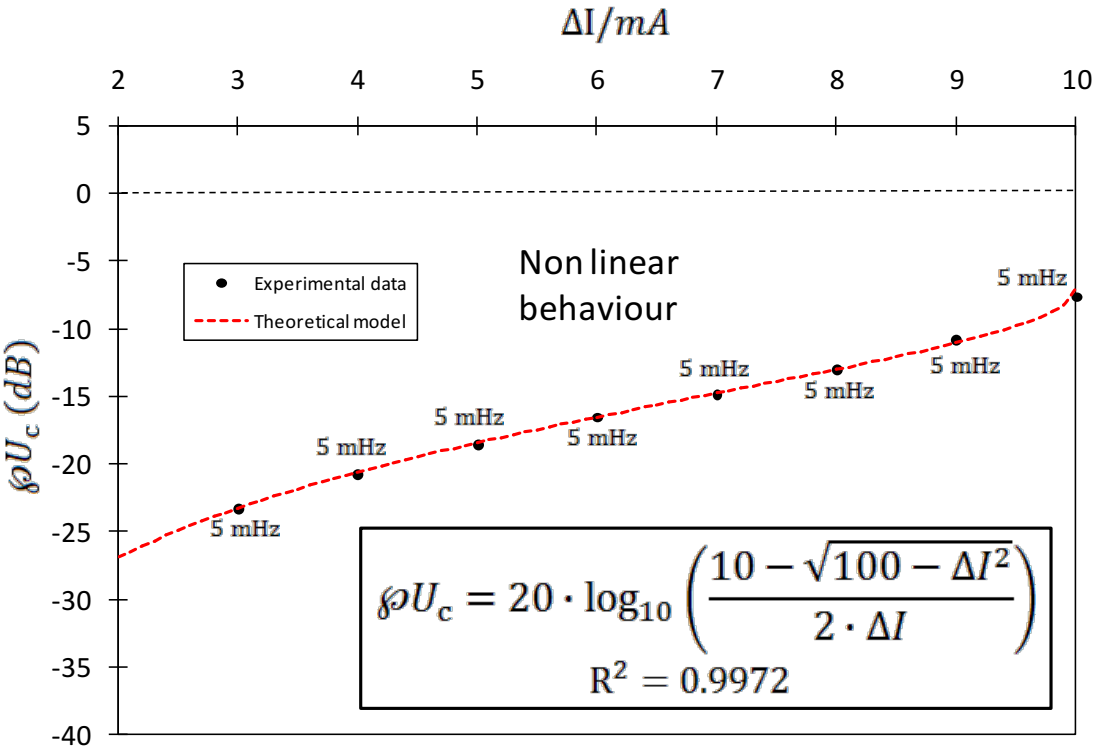

Figure 9. Nonlinear behaviour zone theoretical model

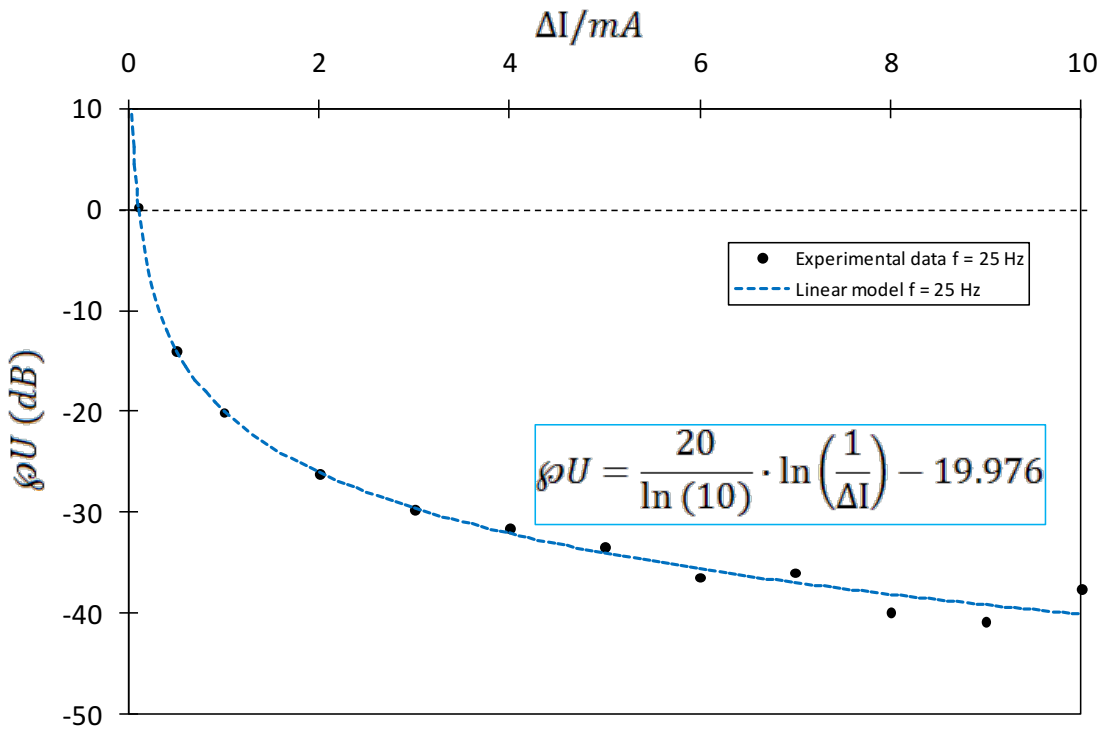

Figure 10. $\wp U$ versus perturbation amplitude curve for an excitation frecuency of 25 Hz

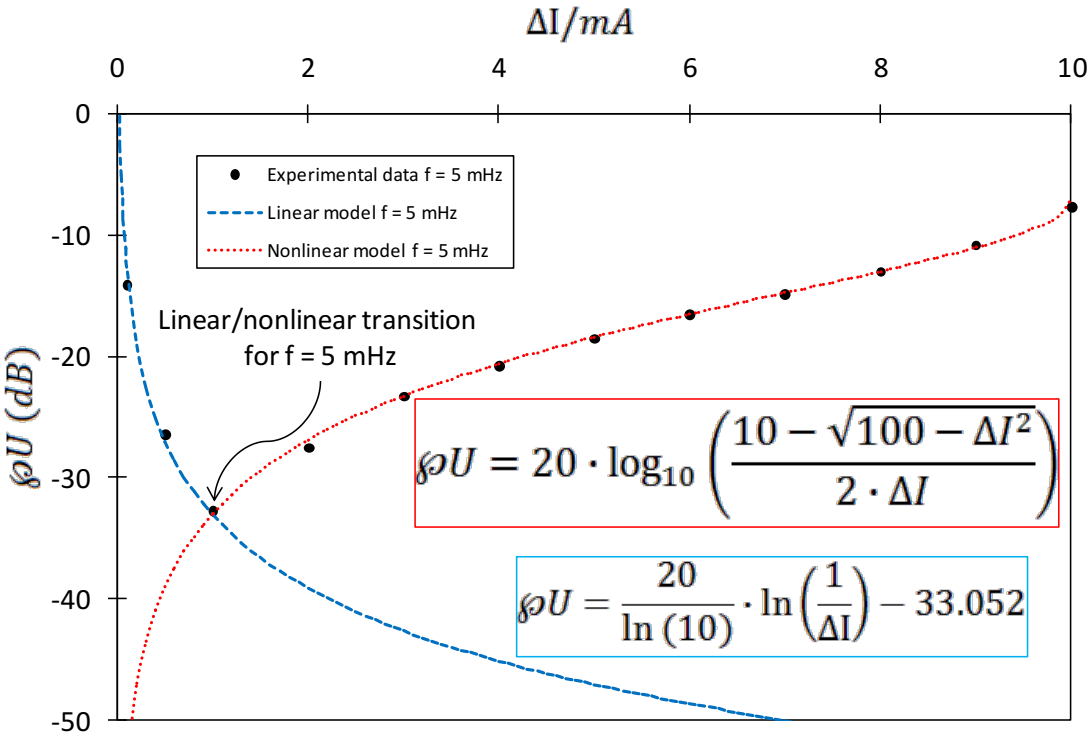

Figure 11. $\wp U$ versus perturbation amplitude curve for an excitation frecuency of 5 mHz

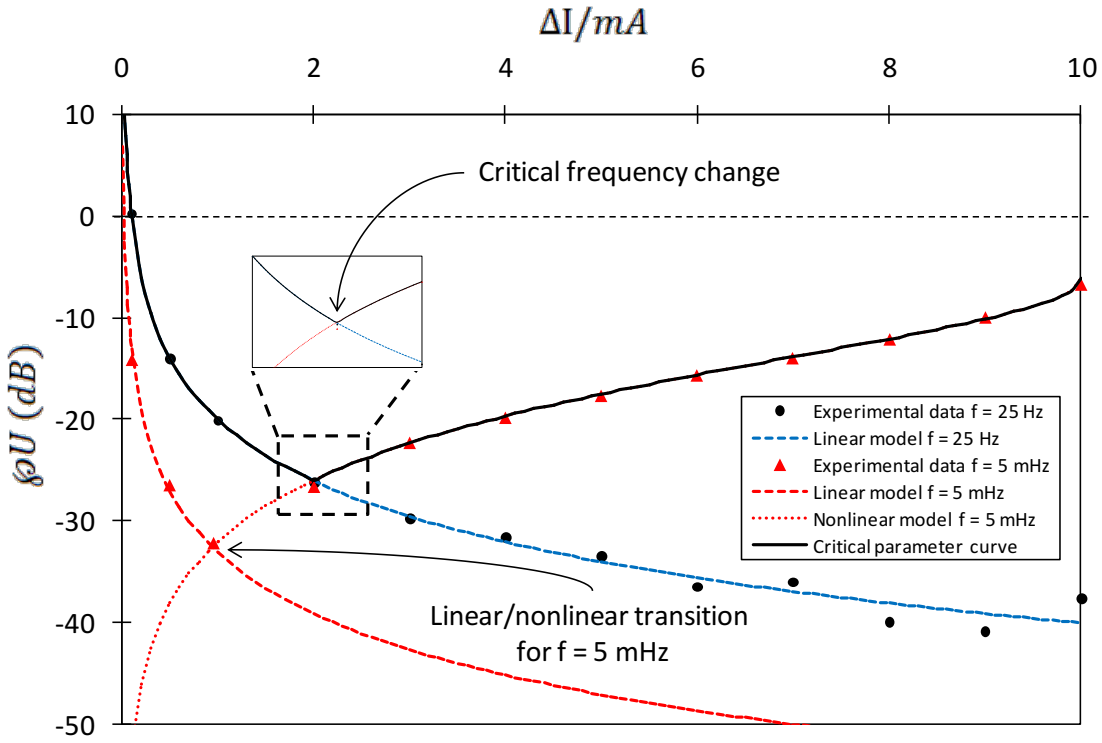

Figure 12. Critical parameter curve and critical frequency change

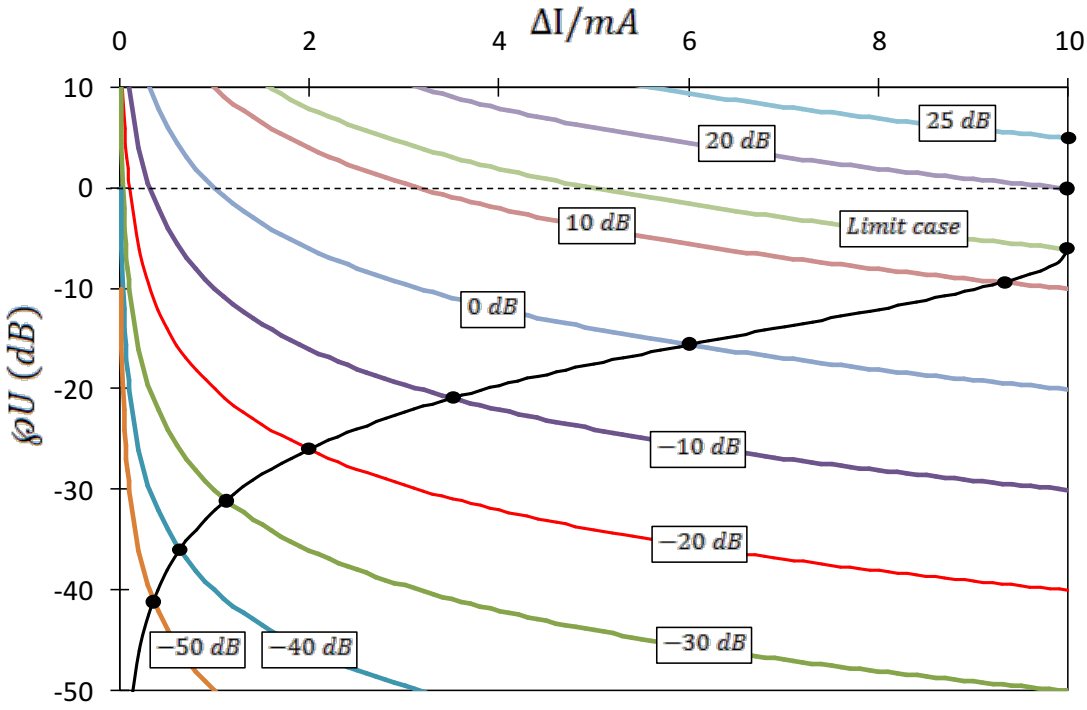

Figure 13. Evolution with the noise related parameter $\left(c_2\left(f_{c\_linear}\right)\right)$ of the intersection point between the model of the linear behaviour zone and the theoretical model of the nonlinear behaviour zone

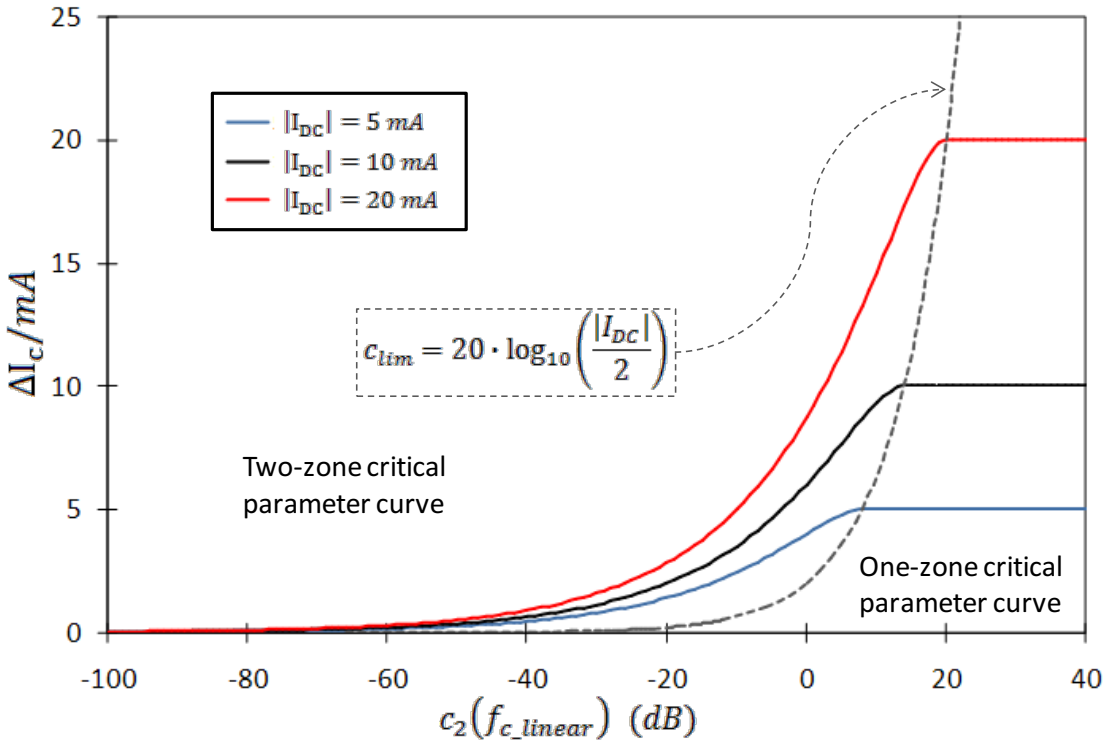

Figure 14. Critical perturbation amplitude versus the noise related parameter of the linear behaviour zone, for 3 different operation points: 5 mA, 10 mA and 20 mA.